University of
Stavanger

FACULTY OF SCIENCE AND TECHNOLOGY

MASTER'S THESIS

Study programme/specialisation:
Petroleum Engineering,
Natural Gas Technology

Spring/ Autumn semester, 2020.

Open / Confidential

Author:
Tamara Hansen

Programme coordinator: Rune Wiggo Time

Supervisor(s): Rune Wiggo Time
Hans Joakim Skadsem and
A.H. Rabenjafimanantsoa

Title of master's thesis:

An Experimental Study of the Enhanced Mass Transfer Process by CO2 Absorption for Carbon Storage in Saline Aquifers

Credits: 30

Keywords:

Carbon Capture and Storage
Pressure decay
Diffusion
Convection
CO2
Saline aquifer

Number of pages: .53.................

+ supplemental material/other: .7.........

Stavanger, 21th July, 2020
date/year

Title page for master's thesis
Faculty of Science and Technology

Abstract

Diffusion of CO_2 into water-based solutions generate an instability at the interface as a result of density differences. The rate of dissolution, the final saturation pressure and the mixing regime caused by convection dominated diffusion are important parameters when evaluating CO_2 storage in geological formations. For this thesis, pressure decay experiments were conducted inside a low pressure (5-7 bar) transparent cylinder-cell with nonsaline and saline water-based solutions containing a pH indicator. In addition, a pressure decay model was derived to study the rate of diffusion and the corresponding final saturation pressure from the experiments conducted. The model was derived with suitable boundary conditions, to keep calculations simple while maintaining high accuracy regarding the measurements. Furthermore, visual interpretations of the mixing regime caused by the enhanced mass transfer mechanism were discussed. This was done in order to understand the contribution of the early and late time convection dominated diffusion of CO_2 into the solutions.

The experiment performed with saline water-based solution in a porous system had a noticeable reduction in the diffusion coefficient. A saturation pressure close to the ambient pressure is desirable to utilise the formation to its fullest potential without exceeding the storage capacity or fracture pressure of the cap rock. In addition, the convection flow showed a significant contribution to the enhanced mass transfer mechanism. The fingers propagated mainly downwards before merging or expanding in the horizontal direction. The observation is important regarding safe and protracted storage of CO_2, where the risk of leakage is highly reduced.

Acknowledgements

I wish to express my sincere appreciation to my supervisors, Professor Rune Wiggo Time, Associate Professor Hans Joakim Skadsem and Senior Engineer A.H. Rabenjafimanantsoa, who has provided me with guidance and expertise throughout the process of writing this thesis.

Besides my advisors, I would like to express my sincere thanks to "Principal analyst/IM Data-management" at Equinor, John Ove Thorsplass, for reading through, and provide valuable and insightful comments.

Table of Contents

Nomenclature

Abbreviations

BTB	Bromothymol blue
CCS	Carbon Capture and Storage
DW	Deionized water
EGR	Enhanced Gas Recovery
EOR	Enhanced Oil Recovery
GHG	Greenhouse gas emissions
IPCC	The Intergovernmental Panel on Climate Change
IR	Infrared radiation
LNG	Liquefied natural gas
LPG	Liquefied petroleum gas
ODE	Ordinary differential equation
PDE	Partial differential equation
UNFCCC	The United Nations Framework Convention on Climate Change
WBS	Water-based solution

List of Symbols

α	Coefficient of thermal expansion $[K^{-1}]$
β	Coefficient of volumetric expansion $[m^3/mol]$
χ	Storage efficiency factor
δ	Atomic charge $[C]$
$\dot{\mu}$	Dipole momentum $[D]$
$\dot{r}$	Distance between molecular center of mass $[m]$
γ	Specific gravity
κ	Wave number $[m^{-1}]$
κ_m	Quantized wave number $[m^{-1}]$

μ	Dynamic viscosity $[Nm/m^2]$
ν	Kinematic viscosity $[m^2/s]$
ϕ	Porosity
ρ	Density $[kg/m^3]$
τ	Positive time constant $[s]$
τ_m	Quantized positive time constant $[s]$
$\vec{J}$	Diffusion flux $[mol/m^2s]$
$\vec{r}$	Position vector
A	Area $[m^3]$
a_m	Fourier coefficient
a_n	Fourier coefficient
At	Atwood number
c	Gas concentration $[mol/m^3]$
D	Diffusion coefficient $[m^2/s]$
d	Diameter of porous media $[m]$
D_T	Thermal diffusivity $[m^2/s]$
g	Gravitational acceleration $[m/s^2]$
h	Gas height $[m]$
h_n	Hydrostatic pressure reference height $[Pa]$
k	Permeability $[m^2]$
K_H	Henry's law constant $[m^3Pa/mol]$
L	Liquid hight $[m]$
l	Glass tube length $[m]$
m	Mass of substance $[kg]$
m	Molecular mass $[kg/mol]$
n	Number of moles [mol]

P	Gas pressure $[Pa]$
P_0	Initial pressure $[Pa]$
P_c	Critical CO_2 Pressure $[Pa]$
P_{atm}	Atmospheric pressure $[Pa]$
P_{sat}	Saturation pressure in bulk volume $[Pa]$
$P_{sat}^{'}$	Saturation pressure in porous medium $[Pa]$
q	Rate $[m^3/s]$
R	Gas constant $[J/molK]$
r	Radius of PVT-cell $[m]$
Ra	Rayleigh number
T	Temperature $[K]$
t	Time $[s]$
V	Volume $[m^3]$
v	Velocity $[m/s]$
V_b	Bulk volume $[m^3]$
V_g	Gas volume $[m^3]$
V_l	Liquid volume $[m^3]$
y	Displacement $[m]$
z	Gas compressibility factor, CO_2

Chemical Symbols

Ar	Argon
CO_2	Carbon dioxide
CO_{32}^{-}	Carbonate ion
H^+	Hydrogen ion
H_2CO_3	Carbonic acid
H_2O	Water

HCO_3^-	Bicarbonate ion
N_2^+	Nitrogen
Na_2CO_3	Sodium carbonate
$NaCl$	Sodium chloride
$NaOH$	Sodium hydroxide
O_2	Oxygen
OH^-	Hydroxide ion

List of Figures

List of Tables

1 Introduction

A clear increase in greenhouse gas emissions (GHG) have been observed the last 150 years. Today, a strong consensus amongst scientists points to anthropogenic activities being the cause of rapid increase in the global average temperature. It is believed that this increase is causing climate changes like extreme weather, rise in sea level and loss in biodiversity (Metz et al., 2005). For this reason, collective obligations such as the Paris Agreement by United Nations Framework Convention on Climate Change (UNFCCC) [1] have been established. The objective of this agreement is to strengthen the global response in order to reduce emissions and keep the increase in global average temperature to well below 2°C above pre-industrial levels (Allen et al., 2018).

Carbon dioxide (CO_2) is the second most important GHG, just after water vapour. In order to achieve these goals, billions of tons of CO_2 must be prevented from being released into the atmosphere every year (The Editors of Equinor, 2018). Several methods have been proposed in order to accomplish these reductions of emission, i.e. renewable energy resources, nuclear power and the use of CO_2 removal techniques such as Carbon Capture and Storage (CCS). The latter stands out by not being a energy source, but a way of controlling CO_2 emissions from fossil fuel-based production during an transition towards a renewable energy mix (Metz et al., 2005). Quoting the former Secretary of State of the Department of Energy and Climate Change, Chris Huhne:

> *Carbon Capture and Storage has a key part to play in ensuring that we can keep the lights on at the same time as fighting climate change. The International Energy Agency has estimated that globally 3 400 CCS plants will be needed by 2050 if we are to meet our critical target (...)* (Di Gianfrancesco, 2016).

CCS is a process where CO_2 is captured and compressed into its supercritical state before transported to a permanent storage site. There are several storage technologies within the field of CCS which are currently researched. Among these are ocean storage, storage in terrestrial ecosystems or by mineral carbonation. In addition, different geological formations have been evaluated for potential sequestration purposes such as hydrocarbon or water bearing reservoirs. However, only CO_2 injections in depleted oil or gas reservoirs as part of tertiary recovery processes (EOR/EGR) have been commercialised by now (Rackley, 2017, pg. 285).

Norway has played an important part in order to meet the collective goals. By increasing investments in renewable energy resources as well as developing models for commercialising CCS, the technology has become a viable solution for decarbonising the energy sector. The Norwegian

---

[1] UNFCCC – The United Nations Framework Convention on Climate Change was established in 1992 at the Earth Summit in Rio de Janeiro, Brazil. The objective is to prevent dangerous anthropogenic (interference) in order to stabilise the greenhouse gas concentration in the atmosphere. It is signed by 189 nations, including Norway

authorities have selected Equinor (previously Statoil) as leading researches on the development of full-scale CCS. This involves all the aspects from capturing CO_2 from the onshore industries, to transportation and permanent storage in geological offshore formations (Ministry of Petroleum and Energy, 2016). The company started permanent storage of CO_2 already in 1996 in the Sleipner gas and condensate field on the Norwegian Continental Shelf, which was the first offshore CCS project in the world (Rackley, 2017). However, in order to implement CCS commercially on a global scale, the evaluated geological formations should not be confined to the few and poorly distributed hydrocarbon depleted reservoirs.

1.1 Objectives

The main focus of this thesis is confined to sequestration of CO_2 into deep geological aquifers. When pumped into the reservoir, a high pressure CO_2 plume will be established above the brine due to buoyancy. With time, CO_2 pressure will gradually decrease as the plume dissolves into the formation water. This causes a instability at the interface due to the fact that the mixture becomes heavier than the underlying brine. The process is favorable, considering that the CO_2 rich brine will flow deeper into the formation due to gravitational effects. However, a risk of leakage will be possible during the time there exist free phase CO_2. Therefore, the enhanced mass transferring mechanisms of CO_2 was investigated by conducting pressure decay experiments. Both bulk volume and porous systems with a nonsaline and a saline water-based solution (WBS) have been studied in order to understand the effect of flow resistance within the system. It is expected that the flow resistance parameters, porosity and salinity, will decrease the diffusion of CO_2 into the solvent significantly, even at small values.

1.2 Organization of the Thesis

All three stages of CCS are introduced in Chapter 2 to provide an overview of the processes involved when storing carbon in subsea formations. The theory introduced in Chapter 3 then relates the physical aspects of CO_2 storage to the diffusion and enhanced mass transfer mechanism, in addition to derivation of the analytical model. Chapter 4 provides a thorough description of the experimental procedures involved to collect data for analysis, including dimensions and apparatus application. The data was then be applied along with the theory for further understanding of the dissolution mechanism and mixing regime. The application and results are discussed in Chapter 5 whereas Chapter 6 summarizes the main observations and results in addition to relevance considering field application.

2 Carbon Capture and Storage

2.1 Capturing the Produced CO_2

The approach for permanently storing CO_2 is divided into three stages where capturing and compressing the gas, mainly from large stationary sources [2], comprises the first step. In the analysis presented in the Intergovernmental Panel on Climate Change (IPCC) Special Report on Carbon dioxide Capture and Storage from 2005, the power and industrial sectors, mainly consisting of fuel combustion activities, industrial processes and natural gas processes, accounted for approximately 60% of the global CO_2 emissions. More than 7 500 large point sources have been identified, thus the potential for capturing from these areas are of primary interest (Metz et al., 2005, pg. 77).

The energy sector from fossil-fuelled power plants are of significant interest since it comprises 85% to 90% of the global electrical power generation (Rackley, 2017, pg. 23). During combustion processes of fossil and biomass fuels, a mixture primarily consisting of nitrogen (N_2), water vapor (H_2O) and carbon dioxide (CO_2), referred to as exhaust gases, are produced. Both H_2O and CO_2 are greenhouse gases, whereas N_2 does not contribute to an increase of the greenhouse effect. The gases are discussed in more detail in section 3.2.

The content of CO_2 in the flue gas may range from 3% to 15% depending on the fuel composition (natural gas combustion emits far less compared to the combustion of coal), amount of oxygen supplied into the combustion chamber and the combustion temperature (Rackley, 2017, pg. 25). Capturing of CO_2 is mainly done, but not limited to, the following ways:

- Post combustion: CO_2 is absorbed from the flue gas by chilled ammonia or by amine solution
- Pre-combustion: partial oxidation reformed to CO_2 and H_2 exhaust by "water-gas shift"
- Oxy-fuel systems: nitrogen is removed from air prior to combustion, resulting in high CO_2 and H_2O concentrated exhaust
- Gasification of carbon-based fuels: high pressure gasifiers turn liquid and solid hydrocarbons into syn-gas before combustion (Norwegian Petroleum, 2020)(Spinelli et al., n.d.)

2.2 Transportation

The second step involves the transportation of the supercritical fluid to the permanent storage sites. For functionality reasons and cost efficiencies, the largest CO_2 producing facilities require a

---

[2] A large point source is defined as emitting > 0.1 Mt-CO_2 per year, since the sources emitting < 0.1 Mt-CO_2/year combined accounted for less than 1% of the emissions from all the stationary sources under consideration (Metz et al., 2005, pg. 78)

transportation infrastructure by pipeline and/or marine, depending on the quantity and distance for transportation. Smaller production sites or deposition in faraway storages may be transported more flexible by ships. Today, transportation of liquified hydrocarbon gas by ships is an already well-established system with different volume capacities. However, transportation of liquified CO_2 is somewhat more demanding.

Both liquified petroleum gas (LPG) and liquified natural gas (LNG) (liquified natural gas i.e. propane and butane or liquified methane, respectively) can be cooled down to its liquid state at close to atmospheric pressure, whereas CO_2 exists only as a gas or solid (dry ice). Therefore, liquefaction of CO_2 requires a pressure above the critical CO_2 pressure $P_C = 73.77$ bar. At this point, the density of CO_2 is at its highest (about 1 200 kg/m^3) which is preferable for optimal utilisation of the carriers. Problems may arise during loading and unloading of the liquid if pressure drops to below the critical point which causes formation of dry ice (Rackley, 2017, pg. 595, 607).

Today, the ships carrying liquified CO_2 are for consumption purposes, and are therefore few and small-sized compared to the vessels transporting LPG and LNG. Accordingly, further development would be required for productive transportation. For long-term projects of large-scale producers, a pipeline network may be a more suitable option (Spinelli et al., n.d.). Norway has long experience with transportation of CO_2 from land to offshore storage, with Equinor being the only operator in Europe that separates and re-injects CO_2 gas offshore. The Sleipner Vest Platform is the biggest contributor with an average injection of one million tonnes per year since 1996. The CO_2 is mainly separated from the Sleipner field and reinjected into the Utsira formation. CO_2 from the Utgard field was added in 2019. In addition, since 2008 the Snøhvit facility has been injecting an average of 0.7 million tonnes/year CO_2 into the Snøhvit field (Norwegian Petroleum, 2020).

Oil and gas are commonly transported by pipelines throughout the world, both on mainland and subsea. The existing CO_2 pipelines are designed for high purity CO_2 transportation at pressures above the critical point in order to reduce corrosion and formation of hydrates. This allows for small diameter pipelines which require less transportation energy and lowers the pressure drops during long distances.

2.3 Aquifer Storage

There are different geological formations viable for sequestering CO_2. Among these are depleted hydrocarbon reservoirs, coal seams and deep saline aquifers. In addition, techniques involving tertiary recovery processes have utilised CO_2 for decades, where hydrocarbon recovery is increased at the same time as CO_2 is sequestrated. Although all processes relay essentially on the same physical and chemical mechanisms, saline aquifers are widely distributed all over the world with large storage capacities and are therefore more accessible. In addition, the aquifers contain high

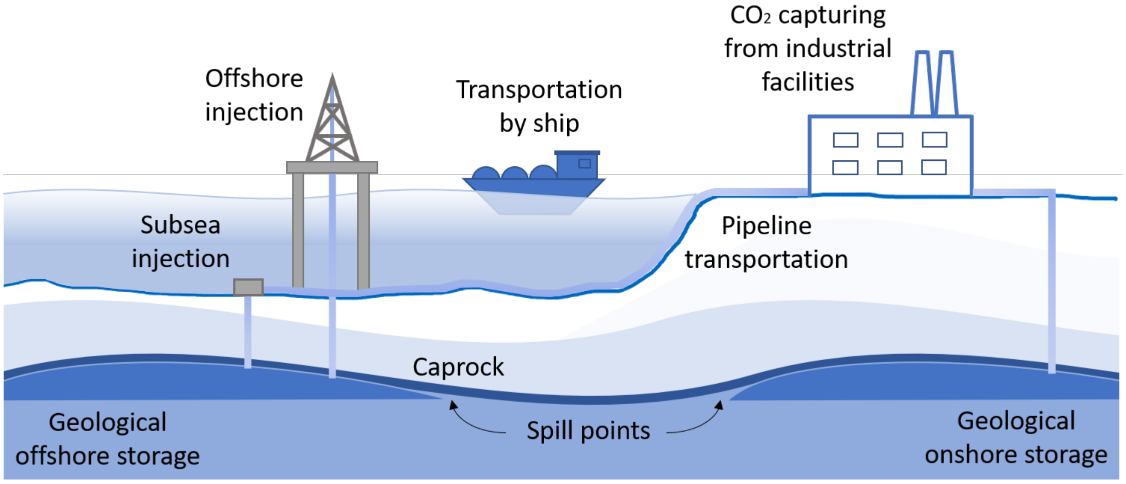

Figure 2.1: Carbon capture, transportation and storage

amounts of dissolved solids and are therefore not viable for drinking, agricultural or industrial purposes (Rackley, 2017, pg. 285-286). In the time of writing, the Utsira formation on the Norwegian continental shelf is the only saline aquifer utilised for CO_2 sequestration in the world.

The formations suitable for sequestration should be large enough to store the CO_2 quantities produced by a power plant throughout its operating lifetime. A simple equation regularly used in the petroleum industries for estimating the storage capacity[3] as mass m of CO_2 of a formation is shown in Equation (2.1) (Bjorlykke, 2015). The equation relates the bulk volume V_b, porosity ϕ, the storage efficiency factor χ, and the net gross ratio of the reservoir to the density ρ of CO_2:

$$m_{CO2} = V_b \phi \chi \frac{Net}{Gross} \rho_{CO2} \tag{2.1}$$

The porosity and permeability of the formation should be sufficiently high at a depth enough to provide a hydrostatic pressure above P_c (usually 800 m below sea level will be sufficient). This allows the fluid to maintain its high density, thus utilising the storage capacity to its fullest and preventing sublimation or vaporization. Nevertheless, an overlaying seal rock with adequate sealing property is also required to prevent leakage of CO_2 due to capillary and buoyancy forces. A comparison between surface conditions, corresponding to 0°C and 1 bar, and at subsurface conditions, corresponding to 35°C and 102 bars, can be made for 1 tonne of CO_2 which occupyes 509 m^3 and 1.39 m^3, respectively (Bentham and Kirby, 2005).

When injected into the aquifer, an interface between the overlaying, highly concentrated CO_2 plum and underlying formation water occurs. The CO_2 will gradually dissolve into the brine, which increases its density and causes convection currents downwards due to gravitational instability. This increases the storage capacity since the underlying brine is pushed upwards. The process

---

[3] Equation (2.1) does not consider the pressure buildup in the reservoir, thus the pressure buildup should be considered in order to not fracture the seal rock.

continues until all the available brine within the aquifer is fully saturated. However, flow resistivity factors such as porosity, permeability and the amount of organic and inorganic dissolved substances e.g. salts and minerals, will affect the diffusivity of CO_2 into the brine. Diffusivity is a critical factor corresponding to the time span it takes for CO_2 to dissolve into the formation water. Consequently, diffusion will also correspond to the time span where the free phase CO_2 can seep out of the aquifer. In order to successfully implement carbon storage operations on a large scale, the physical aspects of CO_2 dissolution process's needs to be fully understood.

3 Theory

3.1 Previous Work

A publication introducing the experimental determination of the diffusion coefficient, called the pressure decay method, was presented by Riazi in 1996. The method is based on the fact that when pressurised gas is in direct contact with a liquid in a closed system, the gas will gradually dissolve into the liquid. This will consequently decrease the pressure until an equilibrium is reached and no more gas can be dissolved i.e. the liquid becomes saturated. The situation is much like in a reservoir where CO_2 is pumped into the formation and a plum is established above the brine. The model has been widely applied due to its simplicity and accuracy for characterisation of absorption and diffusion mechanisms at different operating conditions related to carbon storage (Riazi, 1996). Other studies, involving CO_2-water interactions in PVT-cells based on Riazi's model, have also been conducted in order to understand the processes occurring when CO_2 is used for e.g. tertiary recovery process or sequestration.

Decay experiments in high pressure systems were conducted by Zargham et al. where Riazi's method was applied to study the diffusivity of CO_2 in formation (saline) waters at reservoir temperatures and pressures. The results show that the overall amount of CO_2 dissolution becomes significantly reduced when increasing salt concentration in the solution. However, an increase of CO_2 diffusion at temperatures between 50 and 75°C was observed, assumed to be caused by increased molecular speed (Zarghami, Boukadi, and Al-Wahaibi, 2016).

Farajzadeh et al. studied the differences between diffusion coefficients and the measured effective molecular diffusion of CO_2 at different time intervals in high pressure systems. These diffusion coefficient are fitting parameters with no physical meaning, however highly important regarding the transfer rate for CO_2 in a reservoir. At shorter intervals, the coefficients were two orders of magnitude larger compared to the measured data, while long-time diffusion coefficients were comparable. Both water and hydrocarbon based solutions were tested, and the enhanced mass transfer was assumed to be due to advection currents caused by the increased overlaying density of water containing dissolved CO_2 (Farajzadeh et al., 2007).

Experiments were performed by Nazari et al. with water in fluid continuum (bulk volume) and water saturated porous media. This was done in order to determinate diffusion coefficients and the effect of natural convection of CO_2-water systems at different pressures. It was observed that due to natural convection the mass transferring process was enhanced, thereby requiring a diffusion coefficient at early and late stage of the experiments. However, through their analytical model a pseudo diffusion-coefficient for quantification of the dissolution rate at initial time, $t = 0$, was introduced. The model showed good results and matched the experimental data. Thus, through simple calculations they were able to predict the mass transfer by only one diffusion coefficient (Nazari Moghaddam et al., 2012).

Tveteraas has developed analytical models for his master thesis, and investigated different boundary conditions based on the studies presented. His discoveries are consistent with the above, i.e. that pressure decay can not be described exclusively by diffusion, but in a combination with convection at different time intervals (Tveteraas, 2011). The proposed models are simple to use compared to other, more complex proposed models while still showing highly accurate results.

All the experiments presented above were conducted i PVT-cells with similar dimensions. However, the boundary conditions vary with the literature, and are dependent on the fluids used as well as the conditions of each experiment. Most literature assume a constant reference height located at the interface between gas and liquid. In the articles evaluated for this thesis, the published work done by Riazi is the only exclusion where the position is mostly varied with time. Furthermore, the initial concentration at the interface were also varied. The studies done by Zargham et al. and by Farajzadeh et al. consider no gas at initial time throughout the liquid interval $0 \leq y \leq L$ while studies done by Nazari et al. and Tveteraas consider instantaneous equilibrium in the uppermost layer $y = 0$. The assumptions made for each system makes analytical solutions simpler to obtain, although not reflecting the actual physical properties correctly. This may lead to errors when applying the models, thus the individual systems and the corresponding results must be evaluated. However, collecting sufficient amounts of data from experiments and ensuring repeatability upon application of the model, inconsistencies becomes easily detected thus validates the integrity.

In this study, a suitable pressure decay model was derived in order to investigate the rate of diffusion from the experiments conducted inside a low pressure PVT-cell. The publications introduced above were all performed in similar geometries, however with different conditions and material. For sequestration purposes, the dissolution mechanisms can be investigated by analytical models ranging from very simple to quite complex, depending on the defined interface boundary conditions and fluids used. The following subsection introduces the most important theoretical relations as well as an analytical model derived for understanding the dissolution process regarding carbon storage.

3.2 CO_2 Structure and Properties

The atmosphere consists of approximately 416 ppm (or 0.0416%) of CO_2 (CO2 Earth, 2020), whereas nitrogen (N_2), oxygen (O_2) and argon (Ar) are the three most abundant gases comprising 78%, 21% and 0.9% of the dry atmosphere, respectively . The reason why CO_2 is considered as a greenhouse gases, is due to its more complex molecular structure and ability to absorb and re-emit infrared radiation (IR) from the sunlight that would otherwise be lost to space.

In order to absorb radiation, molecules must undergo a quantum transition either by movement of its electrons or in its nuclei. The latter is linked to the vibration of molecules, thereby relating to complex molecular structure, i.e. those that have more than one atom. Normal vibrations of these molecules, as illustrated in Figure 3.1 by the arrows, occur in different ways: by (I) symmetric or (II) asymmetric stretching or (III) bending. Argon is monoatomic and does not meet the criteria. However, both nitrogen and oxygen are homoatomic which leads to the second criteria; the molecules must alter their dipole moment $\dot{\mu}$, represented by Equation (3.1) and Figure 3.1 where the vector sum of atomic charge, δ, is multiplied by their distance from the molecule's centre of mass, $\dot{r}$:

$$\dot{\mu} = \delta \cdot \dot{r} \tag{3.1}$$

Due to the symmetric covalent bonding of these homoatomic molecules, there will be no change in the dipole moment in the IR spectrum. However, the situation is different for heteroatomic and polyatomic molecules, which will vibrate upon absorption. Hence, the gases which are considered as greenhouse gases are of the latter structure, such as water vapor (H_2O) and carbon dioxide (CO_2). Figure 3.1 illustrates the vibrations of these two gases. In all three cases, the strong polar structure of the water molecule causes change in in its dipole momentum due to vibrations, while the linear, nonpolar structure of CO_2 only causes change in its dipole momentum for the asymmetric and bending vibration. It is important to mention that each vibration is associated with a broad absorption band (range of wavelengths). Also, molecules can not only undergo vibrations, but also rotations of different rates due to the absorption or by gain or loss of translational energy during collisions with other molecules (Spiro, Purvis-Roberts, and Stagliani, 2012).

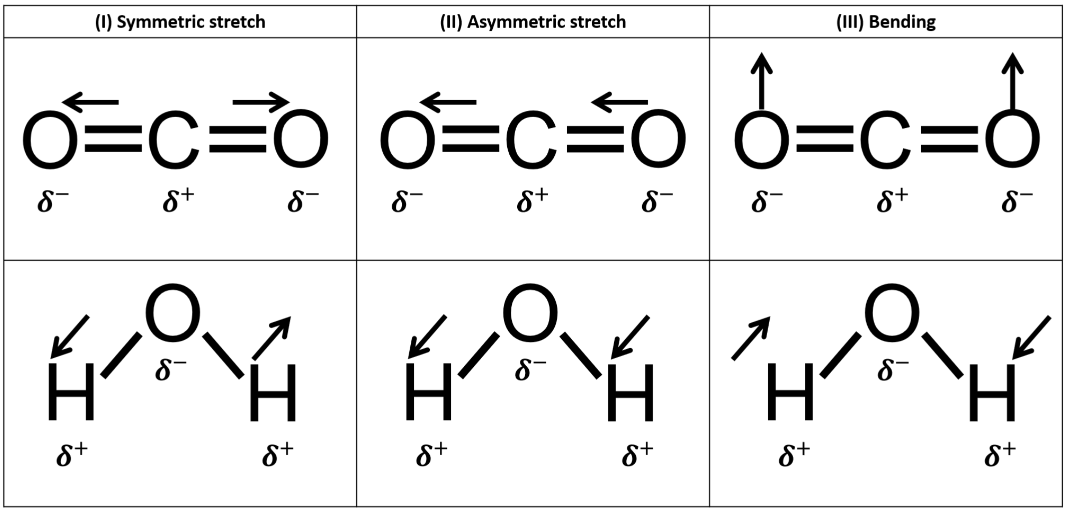

Figure 3.1: Molecular vibrations of CO_2 and H_2O.

3.3 Mass Transfer

Mass may be transferred in different processes through the phase boundaries or within a phase. It is an important mechanism regarding both the capturing and storing process of CO_2.

For this thesis, the mass transfer of CO_2 gas into aqueous solutions was experimentally studied by a PVT-cell. The principles governing the mass transfer mechanisms applied in section 3.5 is presented in the following subsection. The objective is to understand and quantify the transportation process leading to dissolution of CO_2 into aqueous solutions within the cell.

3.3.1 Gas-Liquid Interactions

Solubility of a substance into another is strongly dependent on the atomic structures of the molecules in question. The distribution of electrons shared in a covalent bond in a water molecule creates a strong dipole moment. This makes it capable of dissolving more substances than any other known liquid solvent. The arrangement of atoms enables the molecules to form hydrogen bonds with each other through dipole-dipole interactions. Any other solute with a permanent polar orientation (ions ore molecules) will therefore most likely be soluble in water.

Molecules with no net electrical charge are nonpolar, such as in the case of hydrocarbons, homoatomic molecules and CO_2, amongst other. The distribution of electrons in CO_2 and water is shown in Figure 3.1. As a rule of thumb, nonpolar solutes tend to dissolve in nonpolar solvents, the same way as polar dissolve in polar. However, changes in temperature and pressure may affect the solubility of components with different polarity. Solubility of most liquids and solid solutes are primarily temperature dependent while solubility of gases increases with increasing pressure. The relation between the gas pressure P above a solution is expressed by Henry's law as a function of time:

$$P(t) = K_H c(t) \tag{3.2}$$

where K_H is the Henry's law constant for a given pair of solute-solvent at a specific temperature with the units of $[m^3 Pa/mol]$, and c is the gas concentration as a function of time given in $[mol/m^3]$. Equation (3.2) state that the gas pressure at a specific time is directly proportional to the concentration of gas at the solution interface until equilibrium is established (Osman, 2011, pg. 102-109). This change is explained by the diffusive flux in the next subsection.

3.3.2 Diffusion

Phases in direct contact with etch other will exchange mass due to driving forces such as temperature, concentration or pressure differences. These differences are described by a gradient of the respective physical quantity. In naturally occurring processes, the system will go from a higher to a lower energy state, i.e. from high to low temperature, concentration or pressure. This transfer of energy/mass is described by the macroscopic relative movement of particles with random motion known as diffusive flux, or simply diffusion.

Fick's first law of diffusion can be applied for a system where the concentration of a substance, in this case CO_2 gas, is the driving force with respect to time t or displacement y. When concentration changing with displacement, Fick's first law can be written as:

$$\vec{J} = -D\frac{dc(y)}{dy} \tag{3.3}$$

Equation (3.3) describes the flux of particles in positive downwards y-direction by the J vector in $[mol/m^2s]$ at at the gas-liquid interface $y = 0$, as illustrated by Figure 3.3. The diffusion coefficient D is assumed to be constant for a given pair of species in $[m^2/s]$ at isothermal conditions. However, at $t > 0$ the concentration starts to change as a function of pressure decay. Therefore, a prediction of concentration distribution as CO_2 diffuses into the solution is required. Figure 3.3 illustrates the gas flux through area A which causes concentration change due to molar transfer of CO_2 during a time interval. All this can be summarised into two equations:

$$dn_{CO2} = (J(y) – J(y + dy)) \cdot Adt \tag{3.4}$$

where $J(y + dy) = J(y) + dJ(y)$ where $J(y)$ is simply the same as $\vec{J}$ since we are confined to one direction flux, and:

$$dc(y) = \frac{dn_{CO2}}{Ady} \tag{3.5}$$

By combining both equations and simplifying, an expression of concentration change with time is obtained for the rate of change of flux in y direction:

$$\frac{\partial c(y,t)}{\partial t} = -\frac{\partial \vec{J}}{\partial y} \tag{3.6}$$

which is the first form of Fick's second law. Substituting for $\vec{J}$ from Fick's first law:

$$\frac{\partial c(y,t)}{\partial t} = D\frac{\partial^2 c(y)}{\partial y^2} \tag{3.7}$$

Equation (3.7) is the general form of the diffusion equation in one dimension, predicting the concentration change due to diffusion with respect to time (The University of Utah's College of Engineering, n.d.). For diffusion in two or more dimensions, the equation becomes mathematically analogues to the heat equation:

$$\frac{\partial c(\vec{r},t)}{\partial t} = D\nabla^2 c(\vec{r}) \tag{3.8}$$

where $\vec{r}$ is the position vector, e.g. $\vec{r} = (x, y, z)$ in Cartesian coordinates. The analogy to heat driven flow is proven useful for evaluating convection driven flow, as described in the following subsection.

3.3.3 Convection

Driving forces do not only occur at interfaces, but also within a fluid due to changes in density. The situation is known as convection and is caused by internal differences in temperature or pressure. A classic example is heating water in a kettle. The change in density when a fluid is heated from underneath at constant pressure, causing a buoyancy driven flow which can be described by the Boussinesq approximation:

$$\rho(T) = \rho_i(1 - \alpha \Delta T) \tag{3.9}$$

where ρ_i is the fluid density at a reference temperature, α is the coefficient of thermal expansion and ΔT is the change in temperature during the time interval. The convection flow regime is determined by the dimensionless Rayleigh number:

$$Ra = \frac{\alpha \Delta T r^3 g}{\nu D_T} \tag{3.10}$$

which indicates laminar flow at low Ra, turbulent flow at high Ra, and transient flow in between. Ra is dependent on the geometry of the system where r is the radius of the cell, in addition to the fluid properties where ν is the kinematic liquid viscosity and D_T is the thermal diffusivity.

When CO_2 gas is dissolved into pure water, the following reactions take place:

$$\mathrm{CO_2(g)} \rightleftharpoons \mathrm{CO_2(aq)} \tag{3.11}$$

$$\mathrm{CO_2(aq)} + \mathrm{H_2O} \rightleftharpoons \mathrm{H_2CO_3} \tag{3.12}$$

In this case (and for the reactions of alkaline solutions discussed in section 3.4.1) the products are heavier than the solvent under isothermal conditions, which causes an instability due to gravitational effects when the gas is absorbed from above. The situations is similar to the change in density caused by temperature differences. Figure 3.2 illustrates the situation where a fluid increases its density from above. This causes an instability at the interface known as Rayleigh-Taylor instability, where the stagnation pressure of the denser fluid eventually forces the liquid sideways. The heavier fluid continues to propagate downwards with slightly increasing velocity, until a constant CO_2 concentration is reached throughout the fluid. Equation (3.9) can therefore be modified:

$$\rho = \rho_i[1 + \beta \Delta c] \tag{3.13}$$

where concentration is the driving force, thus ρ_i becomes the fluid density at a reference point and β becomes the coefficient of volumetric expansion in $[m^3/mol]$. Consequently, the Rayleigh number is modified accordingly, relating free convection to diffusion:

$$Ra = \frac{\beta \Delta c r^3 g}{\nu D} \qquad \longrightarrow \qquad Ra = \frac{\Delta \rho r^3 g}{\rho_i \nu D} \tag{3.14}$$

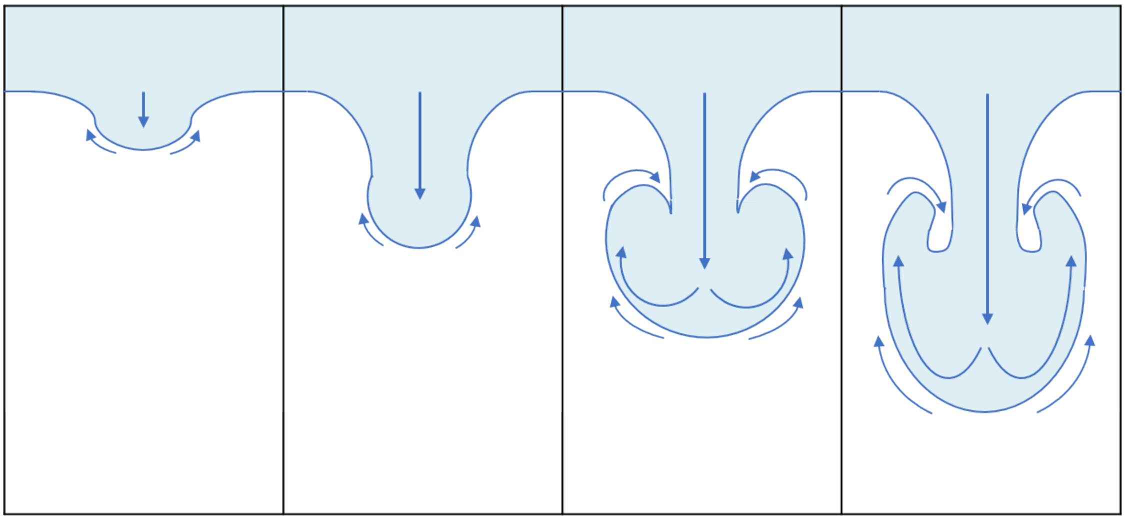

Figure 3.2: Rayleigh-Taylor Instability - developing "mushroom cap" caused by a dense fluid penetrating a lighter fluid due to gravitational effects.

Alternatively, for gas absorption into a liquid saturated porous media, the Rayleigh number becomes a function of both the fluid- and porous media properties:

$$Ra = \frac{k\Delta\rho g d}{\phi\mu D} \tag{3.15}$$

as defined by Khosrokhavar et al. (Khosrokhavar et al., 2014) where k, ϕ and d are the permeability, porosity and characteristic diameter of the porous media, respectively, while μ is the dynamic viscosity of the liquid. Instabilities such as these are affected by different factors including viscosity, diffusivity, surface tension and finite density gradients (Cook and D. Youngs, 2009). The dimensionless Atwood number ($At > 0$) is a parameter which is often associated with hydrodynamic instabilities caused by density driven stratified flow, such as the Rayleigh-Taylor instability:

$$At = \frac{\rho - \rho_i}{\rho + \rho_i} \tag{3.16}$$

It is a simple way to describe the ratio between the sinking fluid due to gravitational effects (or rise due to buoyancy) where $\rho > \rho_i$ for the system described (D. L. Youngs, 1991). The instability is exponentially effected by At, where low values lead to laminar flow and high values cause turbulence.

3.4 Solubility of CO_2 in Aqueous Solutions

As referred to in section 3.3.3, CO_2 dissolved in water, $CO_2(g) \longrightarrow CO_2(aq)$ will have an increase in density which will cause mixing due to gravitational effects. $CO_2(aq)$ is also slightly acidic when dissolved in water. Therefore, in order to improve the visualisation of the transport mechanisms, an alkaline solution of approximately pH = 11 was prepared. The quantities of each component, with the associated characteristics make up the *Solution Base Recipe*:

Table 3.1: Solution Base Recipe

Compound	*Amount*	*Property*
Deionized water (DW)	5 L	pacificated water
5% Sodium hydroxide (NaOH)	3.75 ml	strong base solution
Bromothymol blue (BTB)	35 ml	pH indicator

Each component and mixture were pH tested with a METTLER TOLEDO SevenCompact pH-meter and are listed in Appendix D. The chosen pH indicator has a transition range between pH 6.0 and pH 7.6 where it is yellow at acidic conditions and blue at alkaline. The pH indicator is selected so that it does not have a significant impact on the alkalinity of the solution.

3.4.1 Alkaline Solution

Alkaline solutions are mixtures involving ionic hydroxide compounds dissolved in water. The initial solution, as described above in Table 3.1, will upon the addition of NaOH have a pH greater than 7 due to the increased concentration of OH^-(aq). Strong acids or bases have the ability to completely dissociate in aqueous solution. This means strong acids and bases ionise into hydrogen and hydroxide ions and their corresponding cation and anion, respectively. Contrarily, a weak acid or base will only partly ionise in water (Osman, 2011, pg.12-14) (*Hydroxide* 2017).

When pressurised CO_2 is introduced to the solution, it will react with excess base and form sodium carbonate salt:

$$\mathrm{CO_2 + 2\,NaOH \rightleftharpoons Na_2CO_3 + H_2O} \tag{3.17}$$

It is important to note the amount of NaOH added to the solution is considerably small (approximately $9.90 \cdot 10^{-4} M$), and has the main purpose of increasing the initial alkalinity only (for visual effects with BTB).

CO_2 by itself in the gas phase is not considered as an acid, but becomes slightly acidic when dissolved in water. Reactions involving a strong base and an acidic oxide depends strongly on the concentration of base due to the ability of dissolving completely into OH^-. Therefore, upon dissolution of small amounts of gas there will not be a significant effect on the pH, considering the strong alkalinity of sodium hydroxide. In addition, the produced sodium carbonate salt initially contributes to alkalinity of the solution. However, both the product concentration and the concentration of NaOH is negligible due to their considerably small amounts versus the high concentration of CO_2. Therefore, only the reactions between CO_2 and water will be further evaluated.

3.4.2 CO_2 Dissolution with Water

Increasing the concentration of gas to well above the concentration of NaOH causes a reaction between CO_2 and water to produces bicarbonate ions instead:

$$CO_3{}^{2-} + H_2CO_3 \rightleftharpoons 2\,HCO_3{}^{-} \tag{3.18}$$

which establishes an equilibrium with carbonic acid, and creates a buffer mixture. In the reaction, the carbonic acid works as the weak acid while the bicarbonate is the conjugate base:

$$CO_2 + H_2O \rightleftharpoons H_2CO_3 \rightleftharpoons HCO_3{}^{-} + H^{+} \tag{3.19}$$

The mixture consisting of carbonic acid, H_2CO_3, and amphotheric bicarbonate ions, $HCO_3{}^{-}$ prevents high variations in pH. However, if the concentration of dissolved gas increases to such an extent that the buffer capacity is breached, the solution becomes acidic and the pH indicator turns yellow (Kelland, 2019).

Simple calculations can be used to predict the amount of CO_2 that can maximally be dissolved in water. The main driving force for concentration change is pressure. Thus, as the reactions above continue the driving force decelerates and eventually becomes equal in both phases. At this point the saturation pressure is reached, indicating that no more gas can diffuse into the liquid.

3.4.3 Saline Solution

In order to relate the study of CO_2 diffusion with the rate of mass transfer into formation waters in saline aquifers, the effects of increased ion concentration in WBS were studied. Exact compositions of formation waters varies with local geology. In addition, subsea aquifers evaluated for CCS purposes have high concentrations of dissolved solids. Therefore it was decided to prepare a saline solution according to a standardised brine composition. In order to investigate the effect brine may have on the storage capacity of CO_2, experiments were conducted with the same solution as the one provided in Table 3.1, but with adding 38.4 grams of NaCl per liter of DW before adding NaOH and BTB. The salt provides an ionic strength of 0.657 M. All pH values, before and after conducting the experiment are presented in Appendix D.

A decrease in CO_2 diffusivity is expected in the brine solution due to the increase of ionic strength. Salts do not contribute to direct reactions with water molecules, but dissociate into ions:

$$NaCl \longrightarrow Na^{+} + Cl^{-} \tag{3.20}$$

As discussed in section 3.2 and 3.3.1, water molecules are highly polar. However their ability to dissolve other components are related to temperature and pressure as well as impurities. Therefore, upon the addition of salts, the viscosity of water increases due to hydration of the ions. Consequentially, less CO_2 molecules may dissolve into the solution and an saturation pressure will be reached earlier.

3.5 Analytical Model

The model is based on the assumption that diffusion is the main mass transfer mechanism into a finite liquid height. The boundary conditions were selected in order to keep calculations simple while maintaining high accuracy regarding the measurements.

3.5.1 Boundary Conditions

A simplified model of the PVT-cell at $t = 0$ used to measure and visualise the diffusion process for this thesis is depicted in Figure 3.3. The cell consisted of a CO_2 gas column at initial pressure ($P(t = 0) = P_0$) above atmospheric ($P_0 > 1.013$ bar) on top of the water column. For simplicity, it is assumed that the density of CO_2 only changes with time (t > 0) due to pressure decay, meaning there will be no contribution of water vapor due to phase change from liquid to gas (saturation pressure of water at 25 °C is 0.0317 bar (Çengel, 2012)). This means that the boundary between the phases are considered as constant, thereby disregarding swelling of solution when CO_2 dissolves. The gas behaviour of CO_2 is described by the real gas equation:

$$PV = zn_{CO2}RT \tag{3.21}$$

where the gas compressibility factor $z = 0.98$ is assumed constant. At $t = 0$, the fluids are considered as completely separated, except for the uppermost part of the solution which we assume is instantaneously saturated with CO_2. This means that the concentration of CO_2 is initially zero

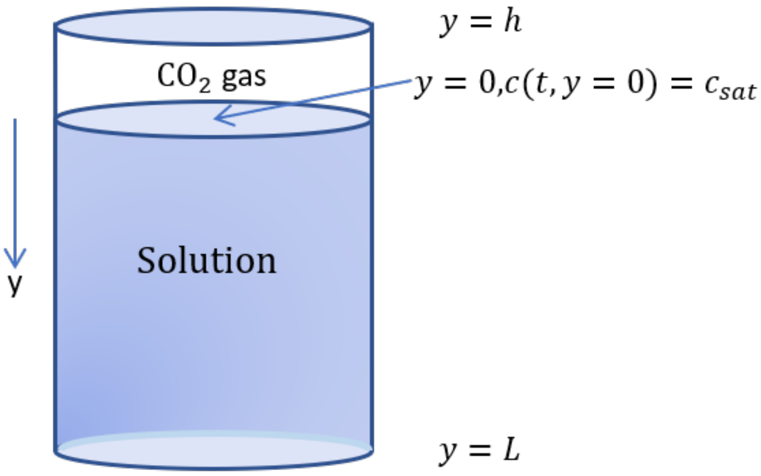

Figure 3.3: Simplified model of PVT-cell

in the liquid phase ($0 < y \leq L$) and maximal at the gas liquid interface ($y = 0$) defined by the initial gas pressure. Considering Henry's law at all t, the boundaries are defined as:

$$\begin{aligned} c(t, y = 0) &= c_{sat} = \frac{P_{sat}}{K_H} \\ c(t = 0, y > 0) &= 0 \end{aligned} \tag{3.22}$$

Since P is directly proportional to c, an expression for the mass flux of gas ($CO_2(g) \rightleftharpoons CO_2(aq)$) can be derived at the gas-liquid interface, $y = 0$:

$$n_{CO2}(t) = \frac{V}{zRT}\Big(P_0 - P(t)\Big) \tag{3.23}$$

where n_{CO2} is dependent on the gas column pressure at $t > 0$. By differentiating with respect to time and rearranging Equation (3.4), the following relation is obtained:

$$\frac{dn_{CO2}(t)}{dt} = \frac{-V}{zRT}\frac{dP(t)}{dt} = -\vec{J}A \tag{3.24}$$

where $\vec{J}$ is simply obtained from Fick's first law and change in pressure is described by Henry's law. In addition, according to the assumptions, the gas volume and cross section area is constant, thus the gas volume and area is simplified to gas height h. Evaluated at the interface:

$$\frac{dP(t)}{dt} = \frac{-zRTD}{h}\frac{dc(t, y)}{dy}\bigg|_{y=0} \tag{3.25}$$

Equation (3.25) is the upper boundary required to solve Fick's second law of diffusion, relating downwards concentration change by flux with time and pressure. The relation is identical to the one obtained by Nazari et al. (Nazari Moghaddam et al., 2012).

3.5.2 Gas Concentration

The assumption of initial diffusion is based on the fact that there is no CO_2 in the WBS before the experiment starts, with the exception of an infinitesimal instantaneously saturated column at $y = 0$. As the diffusion process starts, the pressure gradient will be rapidly decreasing for a short period of time before the upper layer of the solution is saturated. Since dissolved CO_2 is heavier than the solvent, the mass transfer by convection becomes the main drive force due to mixing.

Fick's second law presented in Equation (3.7) is a partial differential equation (PDE) in one dimension. The equation is linear with a constant coefficient and can therefore be solved by Fourier analysis at the predefined boundaries in section 3.5.1 and at initial conditions. By applying the method of separation of variables, the function product is defined by:

$$c(t, y) = f(t)g(y) \tag{3.26}$$

By substituting into Equation (3.7) and dividing both sides by fg the following relation is obtained:

$$\frac{1}{f}\frac{df}{dt} = \frac{D}{g}\frac{d^2g}{dy^2} \tag{3.27}$$

The time and displacement variables can now be evaluated independently. For the equation to hold, both sides have to be constant. Since the left side of the equation has the dimension of inverse time, we can rewrite both sides with regards to a positive constant τ. Taking into account that diffusion is exponentially decaying, the following relations are obtained:

$$\frac{1}{f}\frac{df}{dt} = -\frac{1}{\tau} \qquad \longrightarrow \qquad \frac{df}{dt} = -\frac{f}{\tau} \tag{3.28}$$

$$\frac{D}{g}\frac{d^2g}{dy^2} = -\frac{1}{\tau} \qquad \longrightarrow \qquad \frac{d^2g}{dy^2} = -\frac{g}{D\tau} \tag{3.29}$$

Equation (3.28) is the well known first-order linear ordinary differential equation (ODE) for exponential growth or decay with the solution:

$$f(t) = f(0)\; exp\left(\frac{-t}{\tau}\right) \tag{3.30}$$

where $f(0)$ is determined from the initial data at $t = 0$. The solution to Equation (3.29) is equivalent to simple harmonic oscillators where the wave number κ is equal to the inverse of $D\tau$:

$$g(y) = g_1 cos(\kappa y) + g_2 sin(\kappa y) \tag{3.31}$$

where g_1 and g_2 are constants determined from the boundary conditions. In order to satisfy the boundaries at $t = 0$, g_1 must be equal to zero at the upper boundary, $y = 0$. The boundary conditions also demand that the derivative of the concentration is equal to zero at the bottom of the cell. Therefore, κ will only be equal to zero at specific cases:

$$\kappa_m = (2m+1)\frac{\pi}{2L} \qquad m \in \mathbb{N} \tag{3.32}$$

This implies that τ is quantized as well:

$$\frac{1}{\tau_m} = D\kappa_m^2 = D\left((2m+1)\frac{\pi}{2L}\right)^2 \tag{3.33}$$

The separation of variables provide infinitely many distinct solutions of Fick's second law at the defined boundaries. Defining $a_m = g_2 f(0)$ for each Fourier mode, the full expression of the function product becomes:

$$c(t,y) = a_m exp\left(\frac{-t}{\tau_m}\right) sin(\kappa_m y) \tag{3.34}$$

Since Fick's second law is linear, the most general solution to Equation (3.34) will be a superposition of all the specific solutions given by the infinite sum:

$$c(t,y) = a_0 + \sum_{n=0}^{\infty} a_n exp\left(\frac{-tD(2n+1)^2\pi^2}{4L^2}\right) sin\left(\frac{(2n+1)\pi y}{2L}\right) \tag{3.35}$$

Where a_0 is determined at the upper boundary at $t = 0$:

$$c(t, y = 0) = a_0 = c_{sat} \tag{3.36}$$

and a_n is determined by the gas concentration in the liquid column $0 < y < L$ at $t = 0$:

$$\int_0^L c(t=0,y)dy = a_n = -a_0\frac{4}{(2n+1)\pi} \tag{3.37}$$

The complete derivation of a_n is provided in Appendix C. The final solution describing the gas concentration as a function of time and solution depth:

$$c(t,y) = c_{sat} - \sum_{n=0}^{\infty} c_{sat}\frac{4}{(2n+1)\pi}exp\bigg(\frac{-tD(2n+1)^2\pi^2}{4L^2}\bigg)sin\bigg(\frac{(2n+1)\pi y}{2L}\bigg) \tag{3.38}$$

3.5.3 Diffusion Coefficient

The diffusion coefficient D is required at each of the mass transferring stages, namely for the early and late diffusivity.

By integrating equating (3.25) obtained from material balance at the upper boundary, the change in pressure by diffusion is given by:

$$\int_{P(t)}^{P_{sat}} dP(t) = \frac{-zRTD}{h}\int_t^{\infty}\frac{dc(y)}{dy}\bigg|_{y=0} \tag{3.39}$$

while the change in concentration at the interface can be obtained by differentiating Equation (3.38) with respect to y:

$$\frac{dc(t,y=0)}{dy} = -\sum_{n=0}^{\infty} c_{sat}\frac{2}{L}exp\bigg(\frac{-tD(2n+1)^2\pi^2}{4L^2}\bigg) \tag{3.40}$$

Substituting Equation (3.40) into Equation (3.39) and integrating over the domain yields:

$$P(t) - P_{sat} = \boldsymbol{\gamma}\frac{8}{\pi^2}c_{sat}\sum_{n=0}^{\infty}\frac{1}{(2n+1)^2}exp\bigg(\frac{-tD(2n+1)^2\pi^2}{4L^2}\bigg) \tag{3.41}$$

where $\boldsymbol{\gamma} = LzRT/h$. By rewriting the equation with regards to the real gas law at the upper boundary (Equation (3.23) when $P(t) = P_{sat}$), the relation between the pressures are obtained:

$$P(t) - P_{sat} = \frac{8}{\pi^2}(P_0 - P_{sat})\sum_{n=0}^{\infty}\frac{1}{(2n+1)^2}exp\bigg(\frac{-tD(2n+1)^2\pi^2}{4L^2}\bigg) \tag{3.42}$$

Figure 3.4 shows n as function of time for some representative values for L, D and t. As can be seen from the graph, when $t \to \infty$, the infinite series will converge towards a single value and is therefor evaluated at n=0 only:

$$P(t) - P_{sat} = \frac{8}{\pi^2}(P_0 - P_{sat})exp\bigg(\frac{-tD\pi^2}{4L^2}\bigg) \tag{3.43}$$

Finally, D is obtained by taking the natural logarithm on both sides of Equation (3.43) and plotting the data obtained from the experiments:

$$ln\bigg(\frac{P(t) - P_{sat}}{P_0 - P_{sat}}\bigg) = ln\bigg(\frac{8}{\pi^2}\bigg) - \frac{tD\pi^2}{4L^2} \tag{3.44}$$

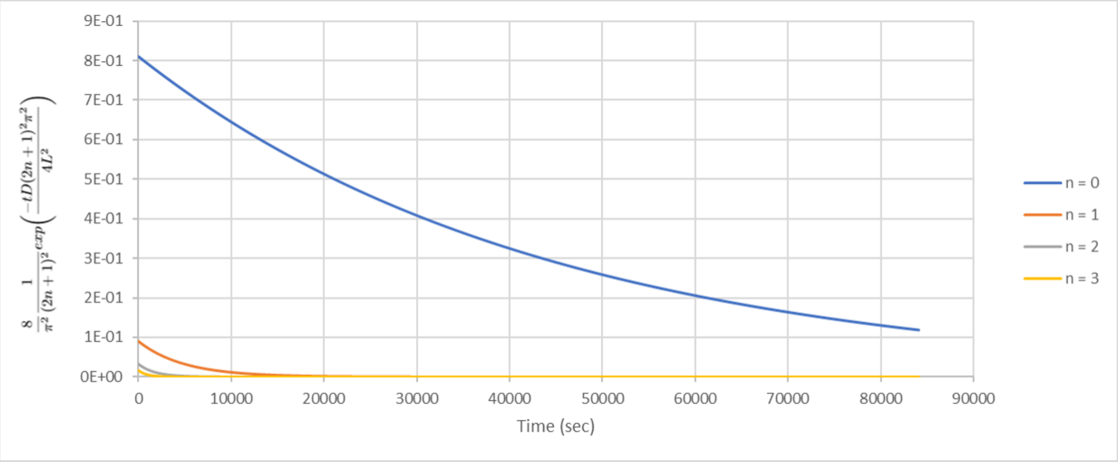

Figure 3.4: Equation (3.42) decreases when $n > 0$

After infinite time, the solution will be completely saturated, meaning no more gas can diffuse into the solution. The theoretical saturation pressure P_{sat} can be calculated by applying the law of mass conservation for Henry's law and the real gas law:

$$P_{sat} = \frac{P_0 K_H h}{K_H h + zRTL} \tag{3.45}$$

If the set of equations are evaluated for a porous medium, the liquid height has to be modified with regards to the liquid space between the matrix. A simple equation used to determine the average porosity of unconsolidated matrices, $\phi = V_p/V_b$, relates the pore volume to the bulk volume, and can be applied for a constant cross section. The theoretical saturation pressure $P_{sat}^{'}$ becomes:

$$P_{sat}^{'} = \frac{P_0 K_H h}{K_H h + zRTL\phi} \tag{3.46}$$

4 Methodology

Different experiments were conducted involving bulk volume, capillaries of different diameters and porous media of uniform grain size. Each set of experiments were performed with a nonslaine and a saline water-based solution (WBS), unless stated otherwise. The objective was to investigate the effects of porosity, permeability and salinity on pressure depletion and mass transfer mechanisms inside a closed system.

4.1 Experimental Setup

Pressure decay of CO_2 gas into WBSs was measured inside a low pressure (5-7 bar) cylinder-cell with a fixed volume of 1380 ml and inside diameter of 66 mm. The cell was placed inside a glass container filled with water. Different porous mediums or capillaries/tubes can be placed inside the cell to study the effect matrix's have on mass transferring mechanisms. Gas and solution may be introduced or extracted at the top or bottom of the cell, depending on the desired gas-liquid ratio. There was no possibility to measure the temperature inside the cell, however it was assumed to be isothermal throughout the experiments due to the water insulating the cell. In addition, the water prevented concavity of pictures due to refraction between liquid and air.

A three-way manifold connected to the top of the cell controlled the gas inlet from the tank and into the PASCO Absolute Pressure Sensor, as illustrated in Figure 4.1. Furthermore, pressure tests were conducted regularly to ensure equipment integrity. This was done by filling the dry cell with air to a desired pressure while constantly monitoring with PASCO Absolute Pressure Sensor. However, it should be noted that each time the valves and top seal was removed, a certain possibility of leakage was probable.

4.2 Experimental procedure

In each set of experiments, a certain volume of solution was extracted from the bottom of the cell at the same time as CO_2 gas was injected through the top valve. The cell was sealed of when the pressure had reached approximately 5 bars. From this point, all decrease in pressure was due to mass transfer from gas into liquid. All changes in pressure were constantly monitored by PASCO Absolute Pressure Sensor. In addition, two cameras were periodically photographing the process as the pH indicator in the solution changed colour due to increased acidity. A scale and a timer was placed within the viewfinder of the camera. In this way, the mass transfer mechanisms could be thoroughly documented.

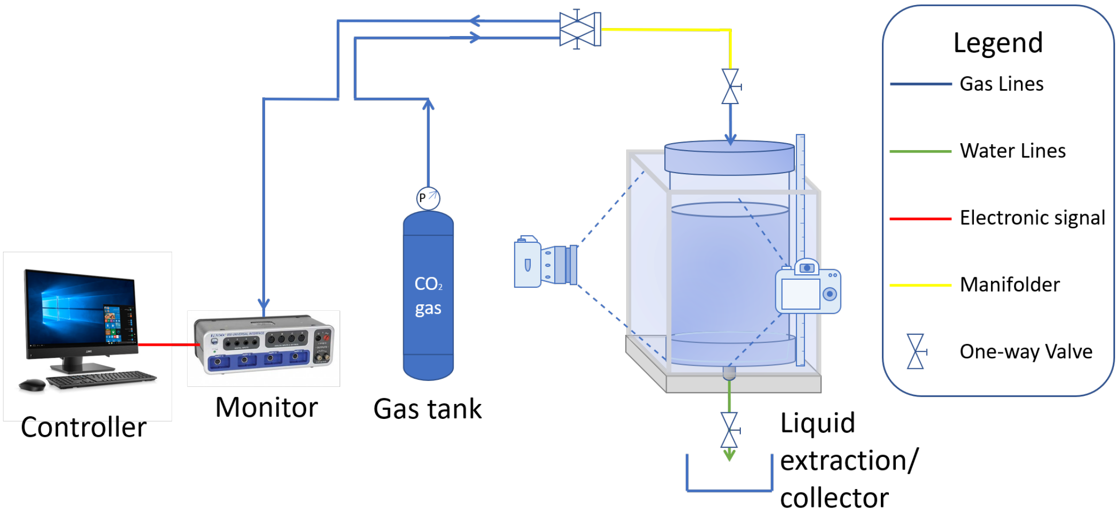

Figure 4.1: CO_2 absorption system

4.2.1 Bulk Volume

The PVT-cell walls were cleaned before firmly sealing the top seal with SGM494 Silicon Grease applied on the tube threads. The grease prevented any gas from seeping out by creating vacuum. After placing the cell inside the container, the cell was completely filled with WBS. This was done by pumping with a piston pump at 10 ml/min in order to prevent air bubbles forming on the cell walls and to assure minimal reactions caused by air. While pumping at a low rate, the solution established a temperature equilibrium with the surrounding water.

The experiment started when CO_2 gas was allowed into the cell from the top while bleeding out approximately 250 ml of solution simultaneously from the bottom. This was done in order to create a gas column on top of the solution. The rapid increase in pressure was monitored at all time and indicated when the desired pressure was reached. At that point the valve on top of the cell was closed off, thus completely isolating the cell volume. This caused an immediate drop in pressure due to the diffusion of CO_2 into the liquid solution.

4.2.2 Impact of Pore Throats

Two transparent tubes (referred to as capillaries) of different diameters were placed inside the cell before firmly sealing the top seal with SGM494 Silicon Grease applied on the tube threads. The capillaries of 10 mm and 4 mm inner diameter and 15 mm and 6 mm outer diameter were used to demonstrate the impact of pore throats on the mass transfer mechanisms. Due to the small reduction in volume, the pressure data will be close to the one obtained from the bulk volume measurements. Therefore, the main interest will be the visual measurements obtained from the colour change in the pH indicator.

Reservoir rocks consists of different sized pores, where the capillary entry pressure is the difference in pressure between the fluids inside and outside the pore space. The different diameters in the capillaries represent the pore throats in a rock matrix where the capillary effects the mass transfer mechanisms, i.e the capillary entry pressure in larger diameter tube throats versus smaller diameter tube throats. The objective was to study the case where a fluid of higher density lies on top of less dense fluids existing inside constrained spaces of different radial entry.

4.2.3 Porous Media

Glass beads of 1 mm average diameter were used to demonstrate the porosity ϕ and permeability k effects on the mass transfer mechanisms. The beads were initially saturated with a alkaline solution in order to remove any acidity on the glass surfaces and to assure a homogeneous water wetness.

A 290 mm long white pipe of 40 mm outer diameter was placed inside the center of the cell before the glass beads were added in order to obtain a 2D effect closest to the cell walls. The pipe should be completely submerged by the saturated beads, both on the inside and outside. This was done in order to avoid any tension on the walls due to pressure differences. Optimal wetness and compaction of the matrix was maintained when adding the beads into the cell containing a small amount of solution. A cap was then placed on the top of the pipe in order to maximize the mass transfer closest to the cell walls. The top seal was then firmly sealing with SGM494 Silicon Grease applied on the tube threads. If seen needed, a syringe or pump could be used to fill the remaining air column inside the cell.

4.2.4 Porosity and Permeability Measurements

Both static and dynamic measurements were performed in order to determine the average porosity of the unconsolidated material, as well as a dynamic measurement of the permeability. The calculations and results are presented in Appendix B.

A graduated cylinder can simply be used to obtain quick and representative measurements of porosity. The cylinder was filled with water to an initial liquid volume V_p before adding glass beads. The maximum matrix volume V_m was reached when all of the beads were wetted and there was no longer a water column above. The obtained bulk volume $V_b = V_m + V_p$ could then be applied in order to calculate the porosity:

$$\phi = \frac{V_p}{V_b} \tag{4.1}$$

Alternatively, a small diameter glass tube of $d = 10$ mm and length $l = 450$ mm packed with the desired matrix material can be used to measure both permeability and porosity. The complete system for both measurements is illustrated in Figure 4.2 where v_1, v_2 and v_3 are valves at their closed position. This measurement allows a higher grade of compaction, unlike the static measurement. However, it is important to mention that visual estimates can affect the results. Therefore, the procedures were repeated at different rates q and pressures P.

The glass tube was connected to a pump at one end with an open outlet at the other. By opening v_2, the beads were sufficiently wetted by pumping water at 499 ml/h through the tube for approximately 1 hour. The porosity was measured by injecting a small amount of color (lissamin rot) at the inlet of the tube. As the colour was pumped through the waterwet matrix, the time and displacement of the colour front was measured. To verify the measurements, the experiment was repeated at different rates until comparable results were achieved. The measured values of displacement were plotted against time, and a linear curve fit was used to obtain the gradient dx/dt. The porosity could then be calculated from the following equation:

$$q = \phi A \frac{dx}{dt} \tag{4.2}$$

When measuring the permeability, v_2 was closed. A flask was hung above the system at an height h_n, and connected at the inlet of the glass tube containing the matrix material. The flask should have a constant volume at all time during the experiment in order to provide a constant hydrostatic pressure into the glass tube. This was possible by pumping water into the flask through opening v_1 and allowing excess water to seep out when maximum volume was reached, as illustrated by Figure 4.2. The experiment started when v_3 was turned to open and the first drop of water seeped out from the glass tube outlet. The rate of water going through the matrix was found by measuring the time and a reference outlet water volume. The experiment was repeated at different h_n. By plotted the rate against h_n, a linear curve fit can be obtained in order to find the gradient q/h_n. The permeability of the matrix can then be calculated by Darcy's law:

$$q = \frac{kA}{\mu} \frac{\rho g h_n}{\Delta l P_{atm}} \tag{4.3}$$

where A and Δl are the tube area and length, respectively, ρ and μ are the water properties, g is the gravitational acceleration constant and P_{atm} is the atmospheric pressure (Rabenjafimanantsoa and Myhren, 2019).

4.2.5 Density and Specific Gravity Measurement of Water-based Solutions and CO_2

The density of the WBS was measured with a 4-digit *DMA* 4100 *M* Density meter from Anton-Paar, while an effusiometer, such as the one illustrated in Figure 4.3, was used to measure the effusion time of CO_2 gas of 99.99% purity. The density meter is a highly accurate tool which

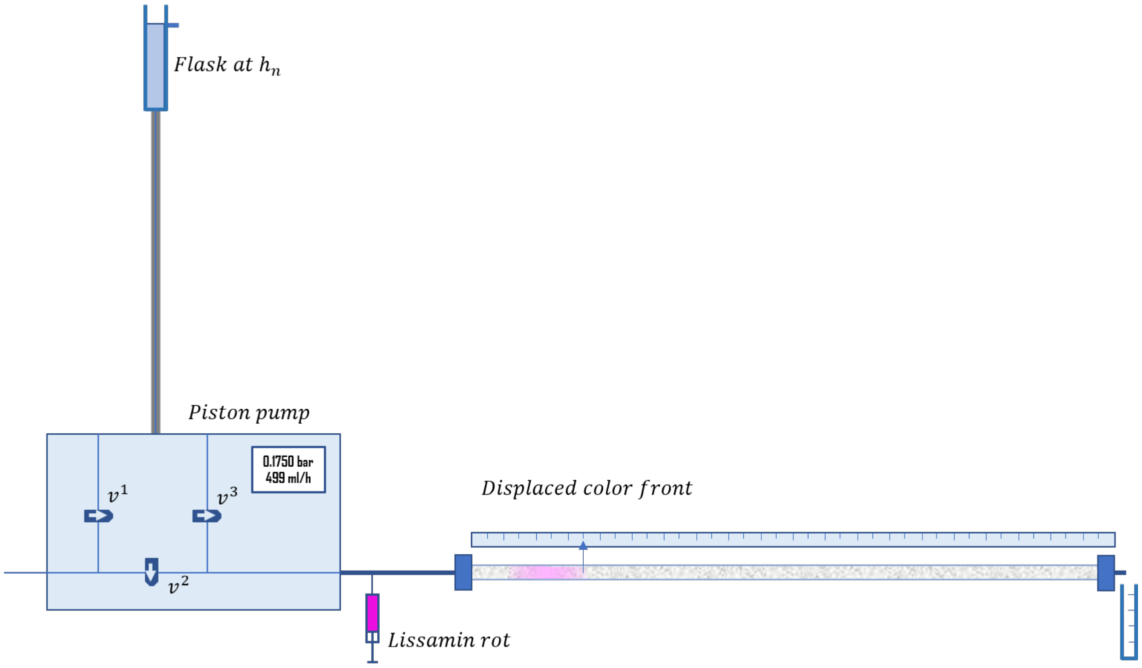

Figure 4.2: Illustration of the porosity and permeability measurement system.

is simple to use and requires only a small amount of the solution. The sample density is highly temperature dependent, and is based on the definition of density as mass per volume:

$$\rho = \frac{m}{V} \tag{4.4}$$

The density meter contains a U-shaped borosilicate glass tube which vibrates at a characteristic frequency when filled with the desired sample. The density of the sample is decided through precise determination of the characteristic frequency and a mathematical conversion (*Anton Paar Instruction Manual DMA 4100 M, DMA 4500 M, DMA 5000 M* 2012). Two different solutions were prepared, a nonsaline and a saline WBS of average 997.1 kg/m^3 and 1023.1 kg/m^3 at 20° respectively, by the *Solution Base Recipe* described in section 3.4.

The measurements and calculations of the gas density are based on Graham's law of effusion:

$$\frac{rate_{ref}}{rate_{gas}} = \sqrt{\frac{M_{gas}}{M_{ref}}} = \frac{t_{gas}}{t_{ref}} \tag{4.5}$$

where the rate is given in volume per unit time and M is the molecular weight of the individual components. Since the effusion of gas and the reference gas (denoted by ref) occurs in the same volume, but with different duration, the rate can be regarded simply as time.

The glass cylinder inside the effusiometer was slowly filled with CO$_2$ gas or reference gas (in this case air) by opening valve B. When the gas reached the bottom of the cylinder, valve B was closed and the system was left for approximately two minutes in order to establish a temperature equilibrium. A thermometer showed the inner temperature of the system at all time. By opening

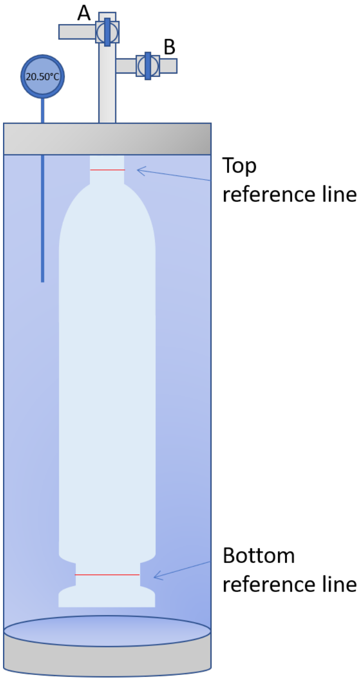

Figure 4.3: Effusiometer illustration

valve A, the gas was allowed to seep out of the glass cylinder through a filter in the top nozzle. A timer was used to measure the effusion time.

The specific gravity $\gamma_{t_2/t_1,P_2/P_1}$ of a gas is a unitless ratio of the gas density to the density of clean, dry air at the same conditions (*Specific gravity* 2018). Specific gravity should always be expressed with associated conditions, however, if the presence of water vapor in air and gas is disregarded, the specific gravity can simply be calculated from the following equation when $t_1 = t_2$ and $P_1 = P_2$:

$$\gamma_{t_2/t_1,P_2/P_1} = \gamma = \frac{\rho_{gas}}{\rho_{air}} \tag{4.6}$$

where air density in $[Kg/m^3]$ at pressure P in $[mmHg]$ and temperature T in [°C] is found by:

$$\rho_{air} = \frac{1.293}{1 + 0.00367 \cdot T} \cdot \frac{P}{760} \tag{4.7}$$

Introducing the equation of kinetic energy $\frac{1}{2}m_1v_1^2 = \frac{1}{2}m_2v_2^2$, Equation (4.5) can be related to Equation (4.6) in the following way:

$$\frac{v_2^2}{v_1^2} = \frac{m_1}{m_2} = \frac{\rho_1}{\rho_2}\frac{V}{V} \qquad \longrightarrow \qquad \frac{t_{gas}^2}{t_{air}^2} = \frac{\rho_{gas}}{\rho_{air}} = \gamma \tag{4.8}$$

where V is an arbitrary unit volume. The average effusion time of each gas measurements were applied with Equation (4.8) where ρ_{CO2} was found to be 0.00199 g/ml at $P_{atm} = 1007.5$ mbar and T = 21.0°C. The measurements and calculations are presented in Appendix A (*Tetthet og relativ tetthet av gass.* 2019).

5 Experimental Results, Application of the Diffusion Model and Discussions

The setup presented in section 4.1 was applied to measure the pressure changes and to record the mixing regime as CO_2 gas diffused into a WBS. Considering the isothermal conditions of the system and the low concentration of NaOH in solution, the change in the pressure gradient was assumed to be due to CO_2 diffusion, and consequently convection within the WBS only. Since concentration is directly proportional to pressure, the pressure data collected can be applied with the derived model to quantify the mass transfer process in each stage, namely early and late diffusion controlled by convection flow.

The mass transfer rate in the cases of bulk volume and porous systems with nonsaline and saline solutions are compared in order to understand the effects of flow resistivity. Table 5.1 includes the initial pressures P_0, volumes of gas and liquid which are measured constants from the experiments in addition to Henry's constant K_H obtained from Henry's law, Equation (3.2), and the real gas law at initial conditions, Equation (3.21).

Table 5.1: Constants from Experimental Data Without Porous Media.

Experiment Label	Pressure P_0	Gas Volume V_g	Liquid Volume V_l	Henry's Constant K_H
Exp 1 Base	5.518 bar	250 ml	1130 ml	2429.073 m^3Pa/mol
Exp 2 Base	4.228 bar	240 ml	1140 ml	2426.579 m^3Pa/mol
Exp 3 Base	5.203 bar	256 ml	1124 ml	2429.073 m^3Pa/mol
Exp 1 Capillary	5.573 bar	250 ml	1032 ml	2429.073 m^3Pa/mol
Exp 2 Capillary	5.841 bar	250 ml	1032 ml	2429.073 m^3Pa/mol
Exp 1 Base+NaCl	5.139 bar	250 ml	1130 ml	2429.073 m^3Pa/mol
Exp 2 Base+NaCl	5.452 bar	250 ml	1130 ml	2429.073 m^3Pa/mol

The *Base* and *Capillary* experiments were conducted with nonsaline WBS while the $Base+NaCl$ experiments were conducted in a saline WBS. Firstly, the experiments without the porous media are discussed. This is done in order to exclude any uncertainties from the porous media. Each set of experiments were plotted for pressure against time. All experimental data are plotted with solid lines while estimated saturation pressures and extrapolations are plotted with dotted lines.

5.1 Experimental Pressure Data in Bulk Volume

Figure 5.1 shows the pressure decay curves obtained for the nonsaline WBS as function of time. The first experiment was abrupt after less than 6 hours and had to be redone. Therefore, the pressure data for *Exp* 1 *Base* will not be evaluated further.

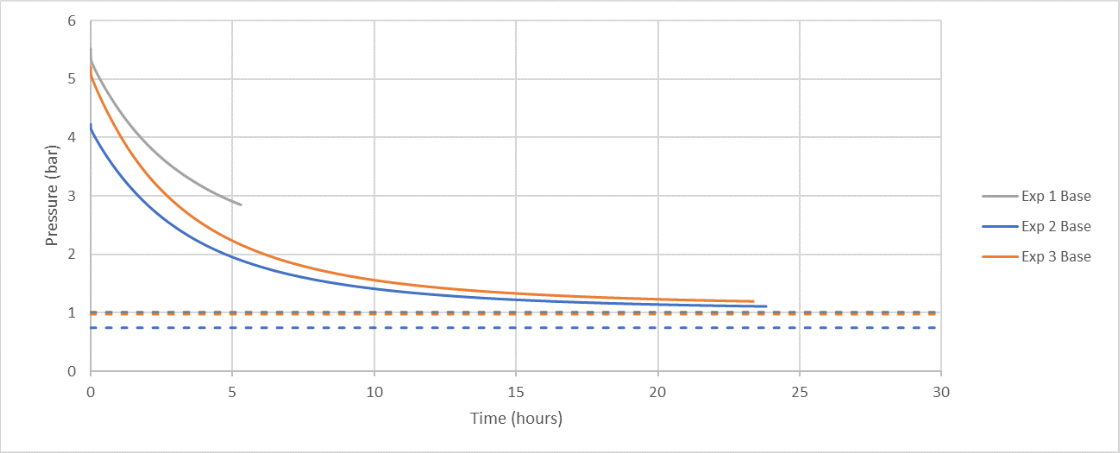

Figure 5.1: Pressure decay in nonsaline water-based solution.

As can be seen from the graph above, *Exp* 2 *Base* and *Exp* 3 *Base* goes towards asymptotic values with time. However, when applying Equation (3.45) the theoretical saturation pressure of 0.745 bar and 0.978 bar, respectively, were obtained as $t \to \infty$. P_{sat} is included in the graph as a straight dotted line for each of the experiments. P_{sat} = 0.745 bars for *Exp* 2 *Base* is much lower than atmospheric, indicating vacuum in the cell. It is assumed that the low initial pressure (P_0 = 4.228 bar) is the reason, imply that the model requires a minimum initial pressure. Therefore, only the results obtained from *Exp* 3 *Base* will be further applied.

The effect of increased ion concentration in WBS was studied in order to relate the rate of mass transfer into saline aquifers. Two experiments were performed with the same saline WBS with 0.657 M of ionic strength to ensure repeatability. The results presented in Figure 5.2 at slightly different P_0 show highly similar trends. The theoretical saturation pressure of 1.001 bar and 0.943 bar for *Exp* 1 *Base* + *NaCl* and *Exp* 2 *Base* + *NaCl* respectively as $t \to \infty$ are considered viable, regarding that the derived model is only dependent on the gas properties. However, it is important to remark that the concentration of salt for these experiments are low. An increase in salt concentration may in reality have a greater effect on P_{sat}, as described in section 3.4.3.

By combining the pressure data for the nonsaline and saline solution in a single plot, the effect of salinity is clearly visible. The decreased diffusivity of CO_2, even at relatively low salinity, is believed to be caused by increased resistance of CO_2 flow within the liquid, i.e. the effect from convection flow is decreased as a result of an increased ionic strength. The principle was discussed

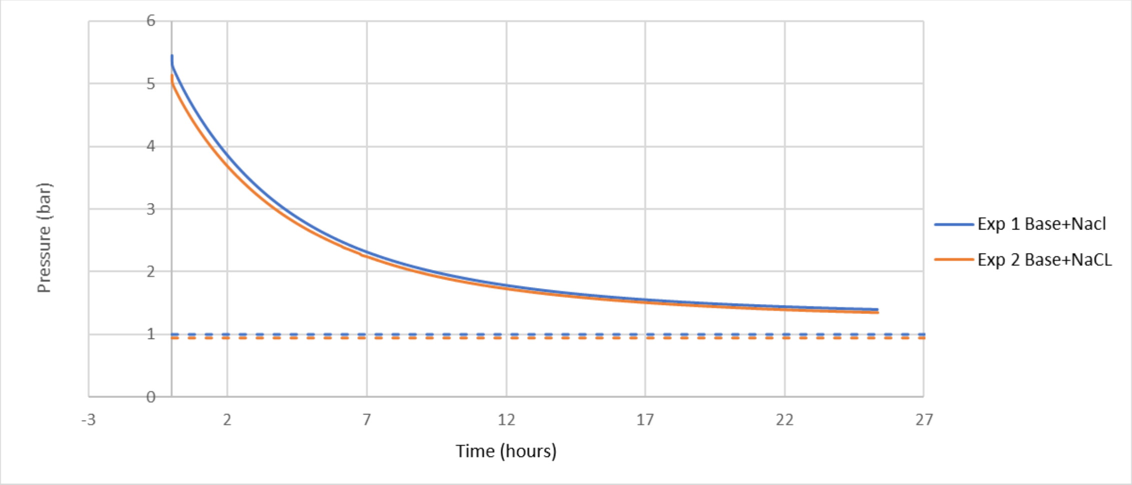

Figure 5.2: Pressure vs. Time for Exp 1 and Exp 2 performed with the same saline solution.

in section 3.4.3. When the ionic strength of the solution is increased, the viscosity increases as well due to hydration of ions, thereby attenuating the rate of enhanced mass transfer within the system.

With time, an equilibrium between the phases was established, meaning the solution was saturated with gas and the pressure gradient goes towards zero. Figure 5.3 shows the effect of nonsaline and saline WBS at close to the same P_0, as well as P_{sat} for both cases. From these measurements, it is evident that even small amounts of NaCl affects the diffusion time of CO_2. During the time span presented in Figure 5.3, both curves seem to continuously decrease. Since the experiments are performed with a relative low salinity at low temperature and pressure ranges, the assumption of $P_{sat} = 0.943$ bars as $t \to \infty$ will not be of significant error. However, if considering saline aquifers,

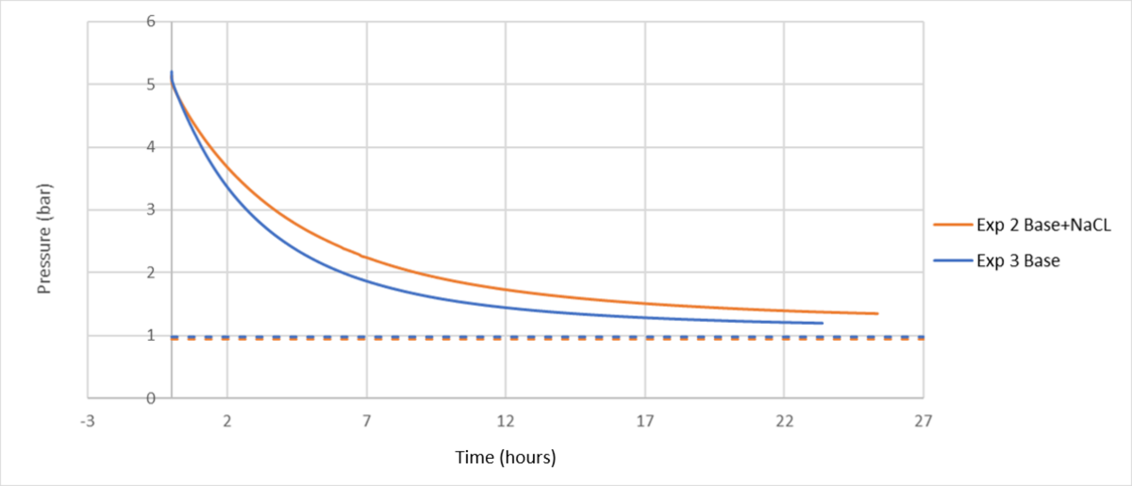

Figure 5.3: Pressure vs. Time for Exp 3 Base and Exp 2 Base+NaCl.

the effect of increased salinity with regards to saturation pressures should be investigated further. The exact content of formation waters differs. Nevertheless the observations from the experiments indicate that higher amounts of dissolved organic and inorganic substances, such as salts and minerals, will affect P_{sat} and thereby the possible amount of sequestered CO_2 to a higher extent. Saturation pressure close to ambient pressure is desirable in order to utilize the formations to its fullest potential, considering the cost of carbon storage field development.

The rate at early and late time of each experiment can be studied by applying Equation (3.44) and plotting against time. Figure 5.4 shows the natural logarithm of the pressure relation as a function of time with the associated linear extrapolated curves of early and late diffusion. The diffusion coefficients D for the saline and nonsaline solutions were obtained from the slope of the straight dotted lines at early and late time and listed in Table 5.2.

Table 5.2: Initial- and saturation pressure with corresponding extracted diffusion coefficients for nonsaline and saline measurements in bulk volume.

	Initial Pressure	Saturation Pressure	Early Diffusion	Late Diffusion
Experiment Label	P_0	P_{sat}	Coefficient	Coefficient
Exp 3 Base	5.203 bar	0.978 bar	$3.50 \cdot 10^{-6} m^2/s$	$4.4 \cdot 10^{-7} m^2/s$
Exp 1 Base+NaCl	5.139 bar	1.001 bar	$2.65 \cdot 10^{-6} m^2/s$	$3.5 \cdot 10^{-7} m^2/s$
Exp 2 Base+NaCl	5.452 bar	0.943 bar	$2.65 \cdot 10^{-6} m^2/s$	$3.5 \cdot 10^{-7} m^2/s$

In order to make the graph more understandable, the x-axis is given in hours. However, the formulas for each trend line is given as function of time in seconds. As can be observed from the listed values, the early diffusion is about one order of magnitude higher compared to the late diffusion. This is due to the assumption of enhanced mass transfer which occurs in the early stage

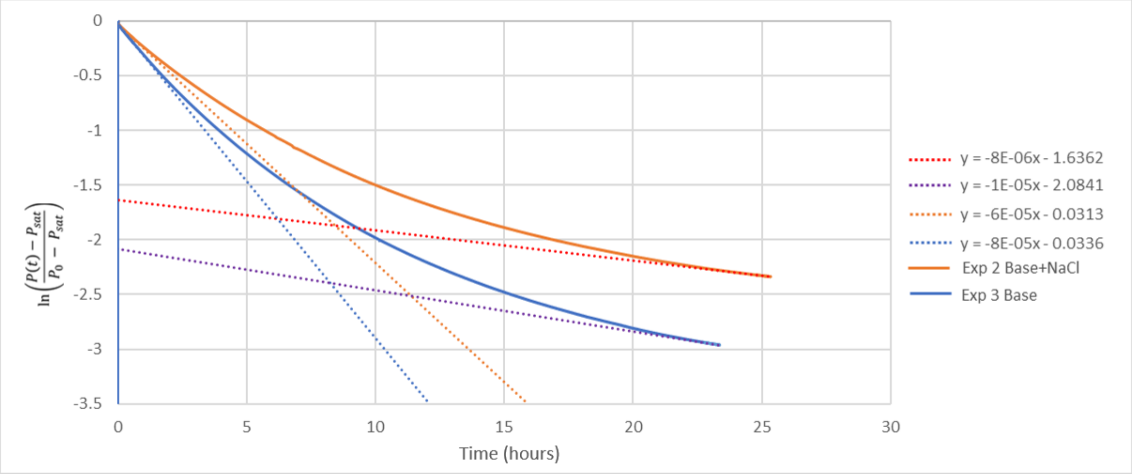

Figure 5.4: Natural logarithm of pressure relation vs. Time for Exp 3 Base and Exp 2 Base+NaCl.

as a result of the difference in solution density. A high diffusion rate is favorable, considering the time CO_2 exists as free gas in the gas column. Again, the difference in diffusivity for the nonsalin and saline solution is clearly visible. The enhanced mass transfer effect becomes overall reduced with increased salinity thereby increasing the time CO_2 can escape due to buoyancy.

5.2 Experimental Pressure Data for Nonsaline and Saline Water-based Solutions in Porous Medium

The measured constants from the experiments with porous media are listed in Table 5.3 where the $Porous$ and the $Porous + NaCl$ experiments were conducted with a nonsaline and saline WBS respectively. The average porosity and permeability of the 1 mm unconsolidated glass beads were measured to be approximately 45% and 23800 mD, respectively.

Table 5.3: Constants from Experimental Data With Porous Media.

Experiment Label	Pressure P_0	Gas Volume V_g	Bulk Volume V_b	Henry's Constant K_H
Exp 1 Porous	6.857 bar	310 ml	1070 ml	2433.23 m^3Pa/mol
Exp 2 Porous	6.140 bar	272 ml	1108 ml	2435.725 m^3Pa/mol
Exp 1 Porous+NaCl	5.625 bar	264 ml	1116 ml	2437.387 m^3Pa/mol
Exp 2 Porous+NaCl	6.155 bar	280 ml	1100 ml	2441.545 m^3Pa/mol

Pressure decay curves obtained in nonsaline WBS are shown in Figure 5.5. Both pressure decay curves show highly similar trends, although shifted relative to each other along the y-axis. When comparing the graph from the porous system experiment to the graphs obtained from a bulk volume system, such as the one in Figure 5.2 it becomes clear that the shift is a direct effect from

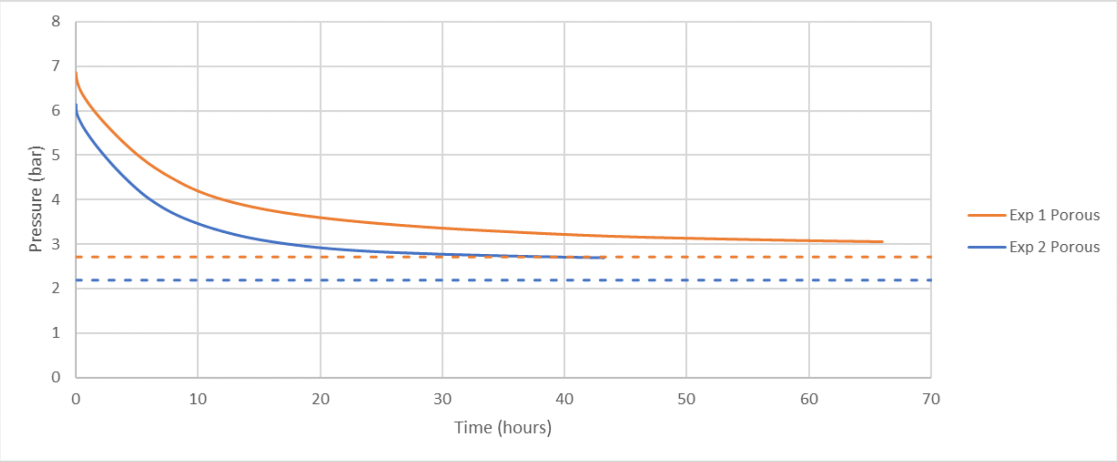

Figure 5.5: Pressure decay for porous media of 23800 mD in nonsaline water-based solution.

the permeability at different P_0. Hence, the porous systems are more affected by P_0 compared to the bulk volume system where the curves in Figure 5.2 goes towards approximately the same P_{sat} after some time, although also starting at different P_0.

Both measurements in Figure 5.5 were still slightly decreasing when the experiments were stopped (at approximately 3.1 and 2.7 bars) due to time limitation. If allowing the measurements to continue, saturation pressures close to the ones obtained analytically (2.712 bar and 2.190 bar, respectively) were likely to have been reached. Some uncertainties, such as the exact porosity, can affect P'_{sat}, which is dependent on initial pressure, gas and liquid height as well as porosity. Nevertheless, the graphs show overall similarities to expected trends, especially when compared to bulk volume results.

When comparing the experimental results from saline solution in porous mediums, it becomes clear that a undetected leakage occurred during $Exp\ 1\ Porous + NaCl$ and will therefore not be evaluated further. Due to time limitations, it was decided to not repeat the experiment. However, the pressure decay measurements for $Exp\ 2\ Porous + NaCl$ were allowed to run for two weeks in order to investigate the achievable saturation pressure. During this time, a pressure of 3.066 bar was reached, although with a continues decline. The assumption of $Psat' = 2.247$ bars as $t \rightarrow \infty$ is therefore considered as viable.

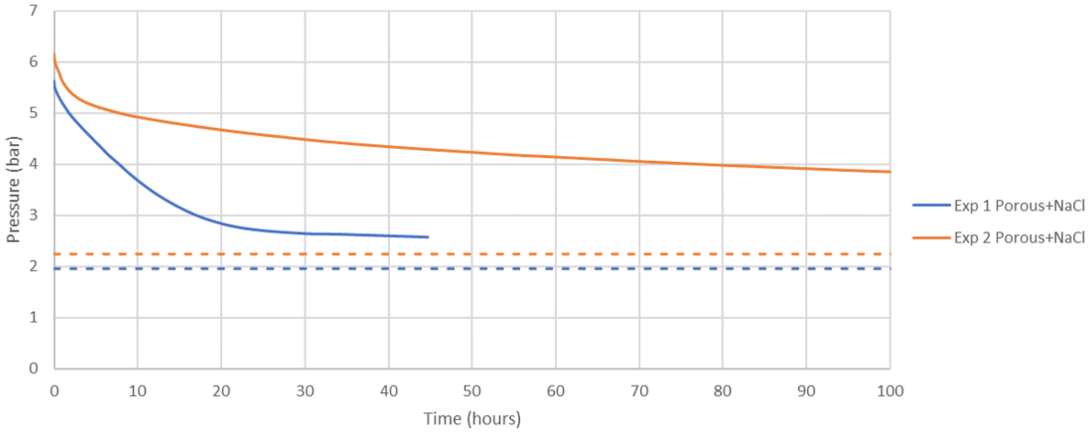

Figure 5.6: Pressure decay for porous media of 23800 mD in saline water-based solution.

The effect of salinity in porous systems becomes clearly visible when combining $Exp\ 2\ Porous$ and $Exp\ 2\ Porous + NaCl$ in the same plot. The experiments were conducted with nonsaline and saline WBS, respectively, at close to the same P_0. The combination of porosity and increased ionic strength decreases the contribution from the enhanced mass transfer, resulting in a much longer late diffusion time span for the porous system. The rate at early- and late time diffusion can be investigated by applying Equation (3.44) with the modified P'_{sat} due to porosity from Equation (3.46). The early and late diffusion coefficients for nonsaline and saline solutions in porous medium are listed in Table 5.4. Unlike all the other experiments, the diffusion coefficient of early- and late time diffusion in the porous medium with saline WBS differed by two orders of magnitude. The observation is noteworthy, considering a high diffusivity rate is favorable whereas in this case it has been reduced. The reduction of the enhanced mass transfer effect at late time should be evaluated when investigating potential water bearing reservoirs for sequestration purposes.

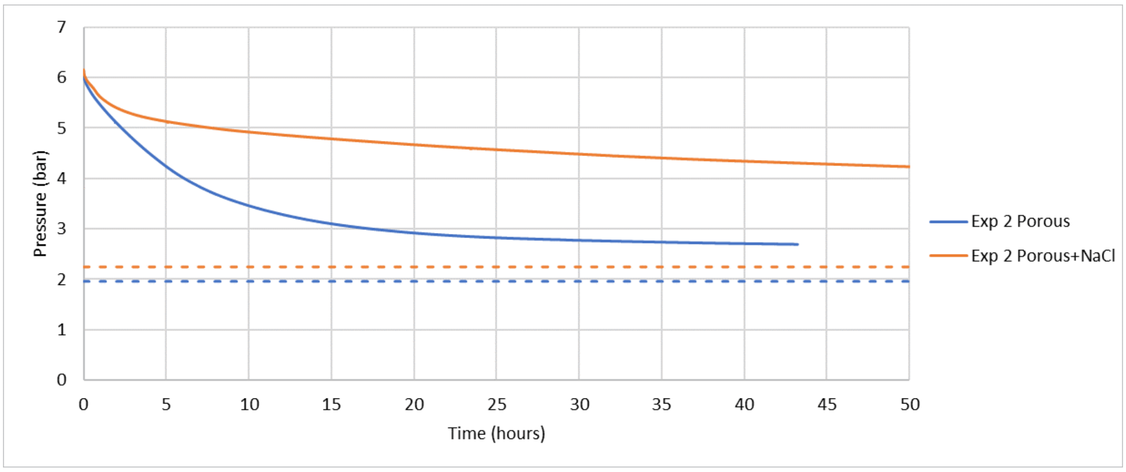

Figure 5.7: Pressure vs. time for Exp 2 Porous and Exp 2 Porous+NaCl.

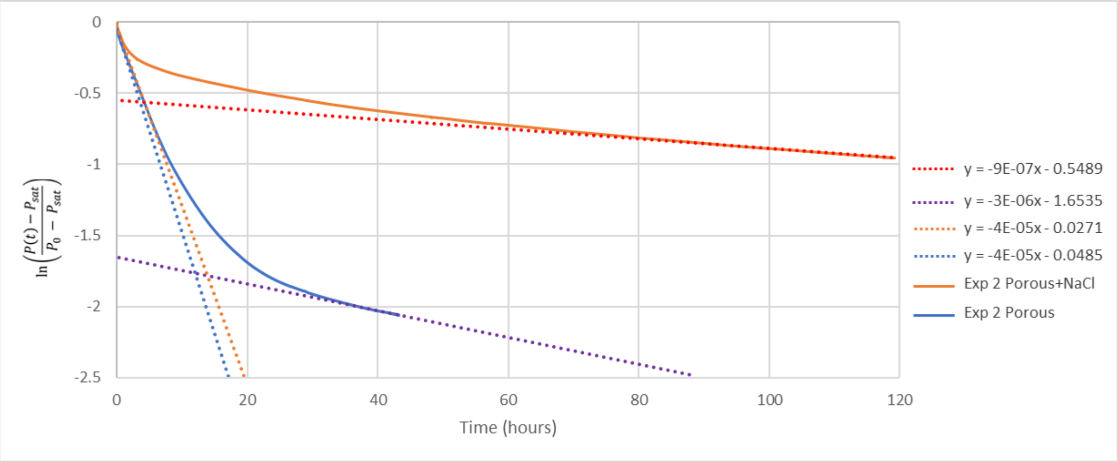

Figure 5.8: Natural logarithm of pressure relation vs. time for Exp 2 Porous and Exp 2 Porous+NaCl (23800 mD)

Table 5.4: Initial- and saturation pressure with corresponding extracted diffusion coefficients for nonsaline and saline measurements in 23800 mD porous medium.

Experiment Label	Initial Pressure P_0	Saturation Pressure P'_{sat}	Early Diffusion Coefficient	Late Diffusion Coefficient
Exp 1 Porous	6.857 bar	2.712 bar	$3.21 \cdot 10^{-7} m^2/s$	$2.40 \cdot 10^{-8} m^2/s$
Exp 2 Porous	6.140 bar	2.190 bar	$3.44 \cdot 10^{-7} m^2/s$	$2.60 \cdot 10^{-8} m^2/s$
Exp 2 Porous+NaCl	6.155 bar	2.247 bar	$3.39 \cdot 10^{-7} m^2/s$	$7.60 \cdot 10^{-9} m^2/s$

5.3 Visual Observations and Experimental Results of the Mixing Regime by Convection Driven Flow

As discussed in the previous section, the pressure decay gradient is much higher initially but decreases with increasing time (one to two order of magnitude). This is true for all of the cases in this study, with associated diffusion coefficients listed in Table 5.2 and 5.4 for bulk volume and porous mediums, respectively. The decay in pressure is directly proportional to the rate of mass transfer, and consequently to the concentration of dissolved gas in the uppermost liquid layer. Figure 5.9 show the pressure decay curve of *Exp 2 Base* in addition to a zoomed in part of the first 250 seconds of the experiments. The graph indicates three stages of diffusion, namely initial diffusion, early- and late convection dominated diffusion. The former stage last for a short period (approximately first 50 seconds) only, in which the uppermost layer goes from close to zero moles of dissolved CO_2 to fully saturated.

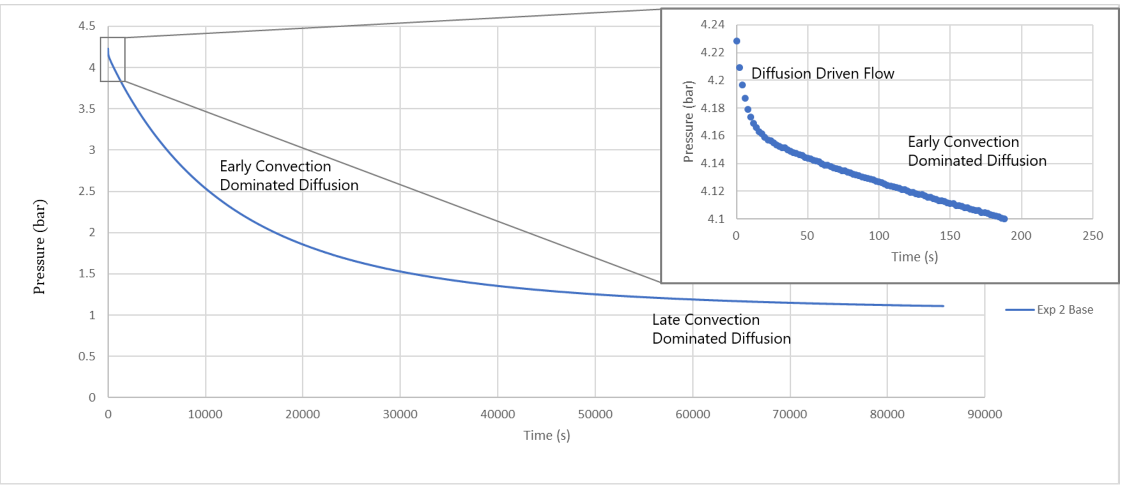

Figure 5.9: Pressure decay in experiment 2 performed with base solution.

The second stage starts where the pressure gradient is changed as a result of natural convection driven mass transfer within the liquid. It is assumed to be caused by the increased density by CO_2 dissolution only. Due to gravitational effects, an instability occurs, initiating a finger-like flow in the downwards direction. The same trend was detected in all of the pressure data. Therefore, the assumption is viable in both bulk volume and porous systems.

The flow regime caused by natural convection can be evaluated by the modified Equation (3.14) of the Rayleigh number for the bulk volume system and from Equation (3.15) for the porous medium. The values listed in Table 5.5 shows the constants applied along with the pressure and early diffusion coefficients from Table 5.2 and Table 5.4. Considering that Ra is evaluated from wide ranges, accurate values of the parameters are not required. Therefore, representative nonsaline and saline unsaturated blue solution were used to determine ρ_i. In addition, μ and ν are obtained for 20°C from tabulated values found in physics books (Engineers Edge, 2020).

Table 5.5: Constants at 20°C, applied when calculating density of the saturated solution.

Constant	Symbol	Value	Unit
Permeability	k	$2.3489 \cdot 10^{-11}$	m^2
Dynamic viscosity	μ	$1.0020 \cdot 10^{-3}$	Nm/m^2
Kinematic viscosity	ν	$1.0040 \cdot 10^{-6}$	m^2/s
Cell radius	r	$3.3000 \cdot 10^{-2}$	m
Compressibility factor[4]	z	0.98	
Porosity	ϕ	0.45	

In the field, CO_2 is sequestrated as a supercritical fluid whereas the experiments were performed with gaseous CO_2 at atmospheric conditions. Performing experiments with CO_2 in its critical state requires a cell which can withstand more than $P_C = 73.77$ bar in a secure way. Therefore, there will be a noticeable amount of CO_2 existing as dispersed gas in the saturated solution ($H_2O\,(l) + CO_2(aq) \rightleftharpoons H_2CO_3(l)$ is strongly shifted to the left). Consequently, when extracted from the pressurised cell, bubbles were formed on the beaker walls and in the density meter. The density of the yellow saturated solution ρ is therefore calculated based on the amount of moles CO_2 entering the blue solution from Equation (3.23) when $P(t) = P_{sat}$.

When determining Ra, the main parameters will be the test pipe geometry, more precisely the radius of the cell. Consequently, the values listed in Table 5.6 will be small. In cases of low At values, the process is visible and often show a high degree of symmetry. Since CO_2 becomes slightly acidic when dissolved in water, a pH indicator was added to the solutions as well as small amount of NaOH (with reference to section 4.2.5 for further detail). It is important to accentuate that the

---

[4] average for 1 to 7 bars

increased alkalinity is meant to enhance the effect from the indicator only, and is not considered to contribute to dissolution rate.

Table 5.6: Measured density of nonsaline and saline WBS at 20°C and the corresponding Rayleigh number for bulk volume and porous systems.

Solution Label	Saturated (yellow) ρ	Atwood number At	Early time Rayleigh number Ra	Late time Rayleigh number Ra
Exp 3 Base	998.9 kg/m^3	0.0009	$4.6794 \cdot 10^5$	$1.4280 \cdot 10^6$
Exp 1 Base+NaCl	1024.8 kg/m^3	0.0008	$2.2112 \cdot 10^5$	$1.6584 \cdot 10^6$
Exp 2 Base+NaCl	1024.9 kg/m^3	0.0009	$2.3461 \cdot 10^5$	$1.7595 \cdot 10^6$
Exp 1 Porous	999.3 kg/m^3	0.0011	0.2318	3.0912
Exp 2 Porous	998.9 kg/m^3	0.0009	1.744	2.3255
Exp 2 Porous+NaCl	1024.9 kg/m^3	0.0009	0.1811	8.0497

5.3.1 Impact of Pore Through Diameters in Mixing Regimes

Two experiments were conducted with different diameter capillaries as described in section 4.2.2. The main interest was to observe how different diameter pore throats were affecting the mass transferring process due to capillary effects. A small diameter tube was expected to have a higher resistance to flow and would therefore maintain the blue solution inside the tube for a somewhat longer period compared to the large diameter tube. Figure 5.10 show a photo pair taken at 13 milliseconds difference, 4 minutes and 44 seconds after the experiment started (i.e. P_0 was reached).

Yellow flow currents were clearly visible on the outside of the tubes, as well as within the tube. However, it was not possible to distinguish from the pictures weather the yellow, higher density solution flowed on the inside or on the outside of the capillaries. The arrows in the pictures point towards the lowest points where yellow solution is observable within the capillaries. The difference is about 3.5 cm, thus ascertaining that the visual measurements and the setup is not sufficient when evaluating the impact of capillary effects on mass transfer mechanisms.

Due to time limitations, it was decide to not pursue with this type of experiment. However, the impact different pore throat geometries may have on the mixing regime is an interesting subject which should be investigated further. Other measuring devises, dyes or pH indicators may be more suitable to obtain a higher degree of contrast in a three dimensional system. Mineralogy is also an affecting parameter, considering CO_2 may react and form precipitation which will ultimately block the pore space. Alternatively, CO_2 may dissolve the rock minerals, thereby increase the pore space which might be favorable.

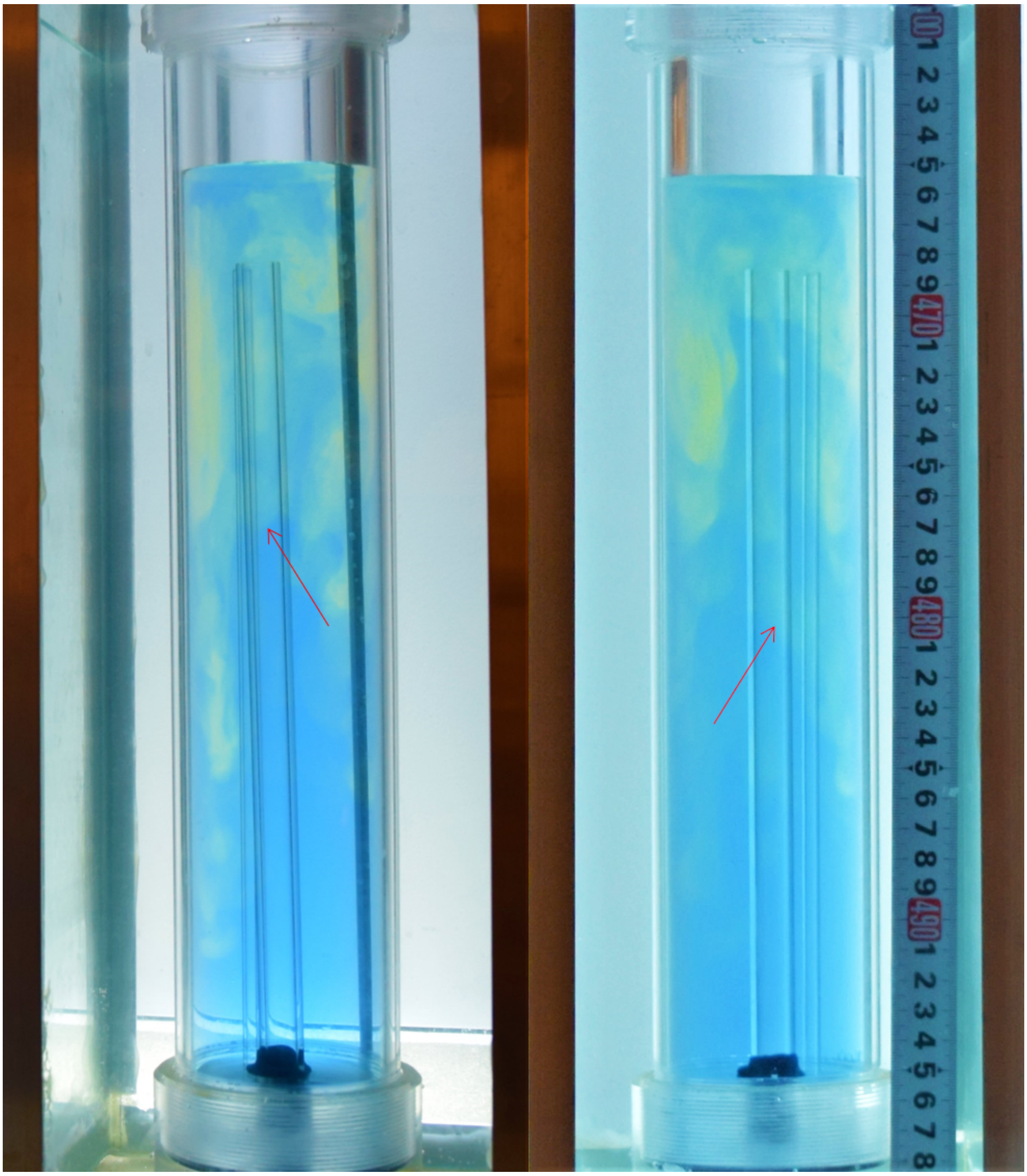

Figure 5.10: Different diameter capillaries for investigation of capillary effects in mass transfer processes. Note that the left image shows mainly the large diameter tube with the right side show a more representative image of the system.

5.3.2 Mixing Regime in Bulk Volume

As the uppermost layer became saturated by CO_2, yellow finger-like flow, caused by convection, became observable in downwards direction due to gravitational effects. The process was recorded with two cameras at 90° angle with a 2 second interval between each capture. Figure 5.11 show a photo pair taken at 1 second difference, 202 seconds after the experiment started (i.e. after P_0 was reached). The red arrows point towards two characteristic mushroom shapes in each picture known as Rayleigh-Taylor instabilities. These were caused by the increasing stagnation pressure at the interface between the dense CO_2 rich fluid (yellow) and the yet unsaturated (blue) solution. As the yellow solution sinks towards the bottom, the blue solution gets pushed upwards. This instability provides unsaturated solution towards the interface, thus increasing the overall dissolution rate of CO_2. Exactly where and when the instability occurs will be unique in each case.

The picture series in Figure 5.12, 5.13 and 5.14 show irregular flow patterns in each case. Fingering may occur in the middle (annular flow) of the cell, mainly along the walls as a liquid film or as a combination of both. The former case was conducted with nonsaline WBS (sequence $A+B$), where the flow propagation was possible to determine by the scale placed inside the glass container filled with water. In this way, the water prevented concavity due to refraction between liquid and air. At $t = 0$ (given in seconds), the maximum pressure of the experiment was reached, thus the system was completely sealed off. Additionally, the red dotted line was placed at the yellow liquid front with reference to $y = 0$ located at the gas-liquid interface (given in mm). The velocity increases from 0 to approximately 0.95 mm/sec as the CO_2 rich fluid propagates downwards, forming vortices due to mixing with the unsaturated blue fluid. The following experiments (sequence $C+D$ and $E+F$) were conducted with saline solutions. The flow occurred mainly along the walls and was therefore not as easily evaluated regarding propagation of the CO_2 saturated fluid. However, the overall color transition from blue to yellow occurred during a longer time span in the saline solutions compared to the nonsaline (approximately twice as fast).

By analysing all three picture series, it is observable that the downwards flow is the dominating factor of the enhanced mass transfer mechanism in bulk volume systems. The yellow fluid starts to propagate along the radial direction mainly after the fingers reached the bottom of the cell i.e. the propagation in the vertical direction is much faster compared to the horizontal. In addition, the solution was first fully saturated in the bottom before propagating upwards. In all three series, some blue solution was visible until the fluids were indistinguishable (again, convection mixing enhances dissolution by bringing fresh, unsaturated fluid upwards).

It is important to state that the time span evaluated is only a small fraction of each experiment and that the mixing regime was continued, although not visible, in the cases discussed in this section. The pressure curves in section 5.1 shows that early diffusion continued much longer in both cases of nonsaline and saline WBS than what was possible to record with the equipment utilised. With time, the contribution from the mixing regime is continually decreasing, i.e. transitioning from early to late diffusion, before the concentration goes towards an overall equilibrium (P_{sat} is reached). Other measuring devices or color indicators may be applied in order to study the continued mixing regime.

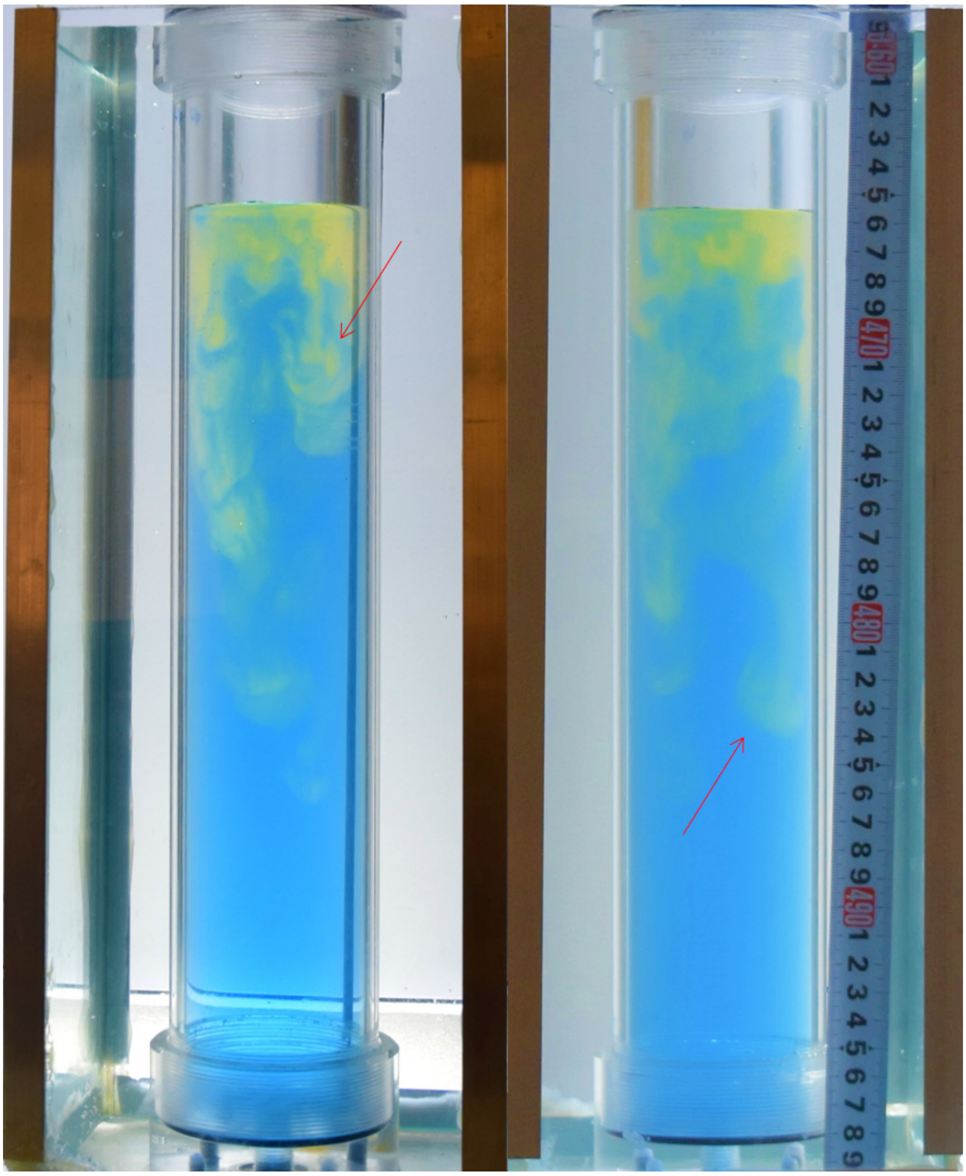

Figure 5.11: Visual observations of enhanced mass transfer by convection driven flow in bulk volume (*Exp* 3 *Base*). The arrows points towards two characteristic mushroom shapes known to appear in connection with with the Rayleigh-Taylor instability.

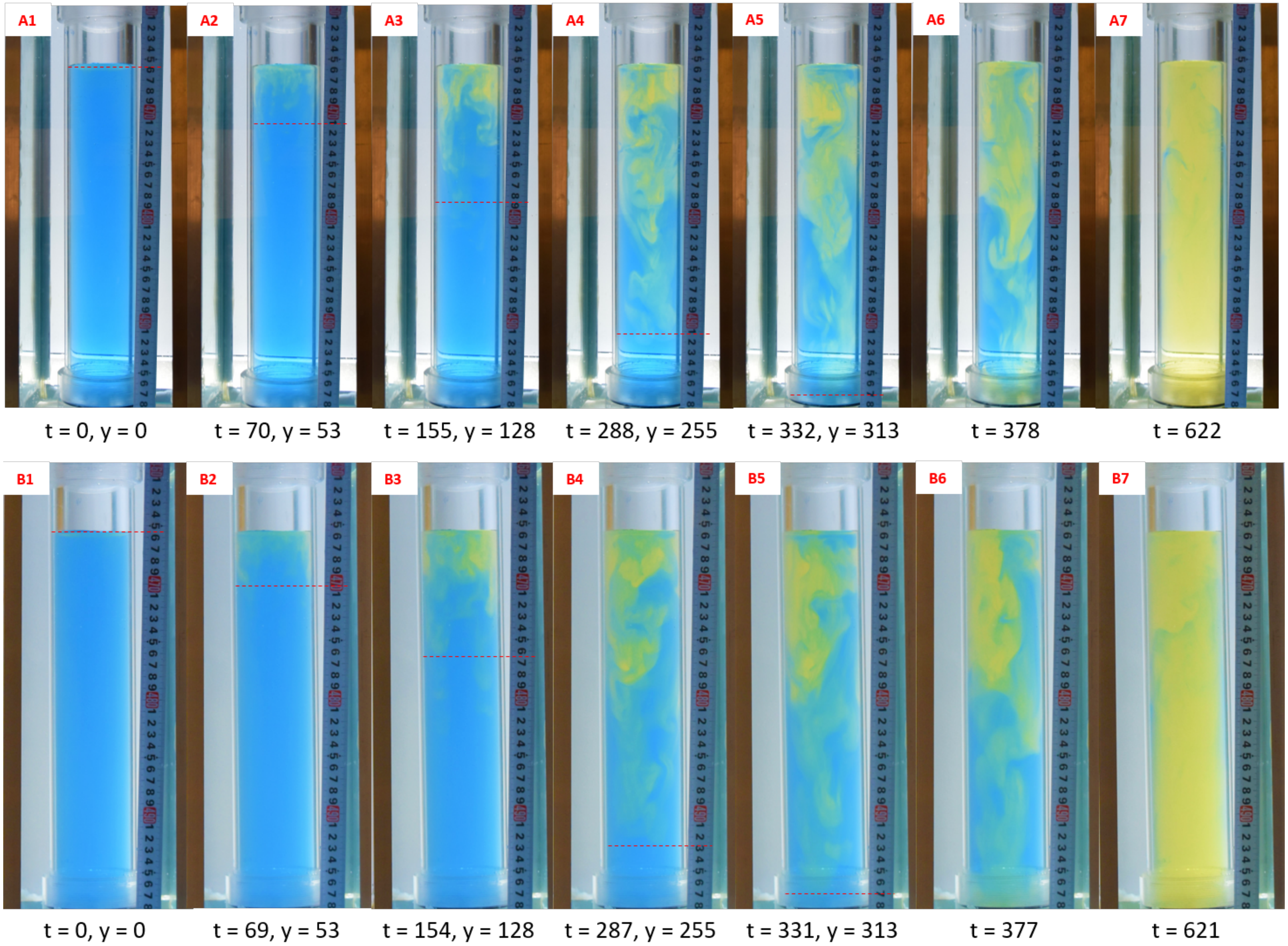

Figure 5.12: Visual observations of mixing regime by natural convection in nonsaline WBS bulk volume (*Exp* 3 *Base*)

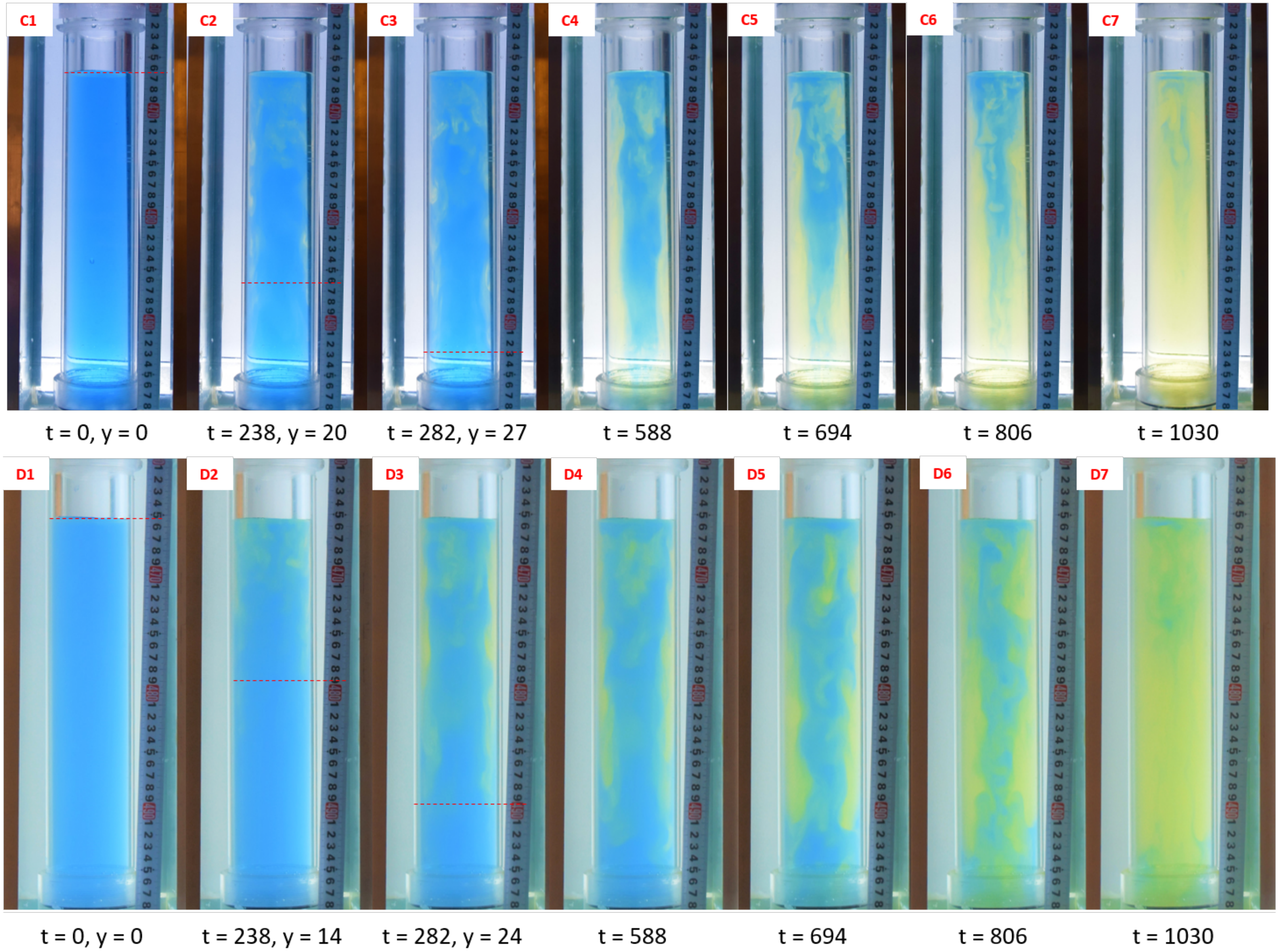

t = 0, y = 0 t = 238, y = 20 t = 282, y = 27 t = 588 t = 694 t = 806 t = 1030

t = 0, y = 0 t = 238, y = 14 t = 282, y = 24 t = 588 t = 694 t = 806 t = 1030

Figure 5.13: (*Exp* 4 *Base* + *NaCl*) - Visual observations of mixing regime by natural convection in saline WBS bulk volume. t [sec], y [mm]

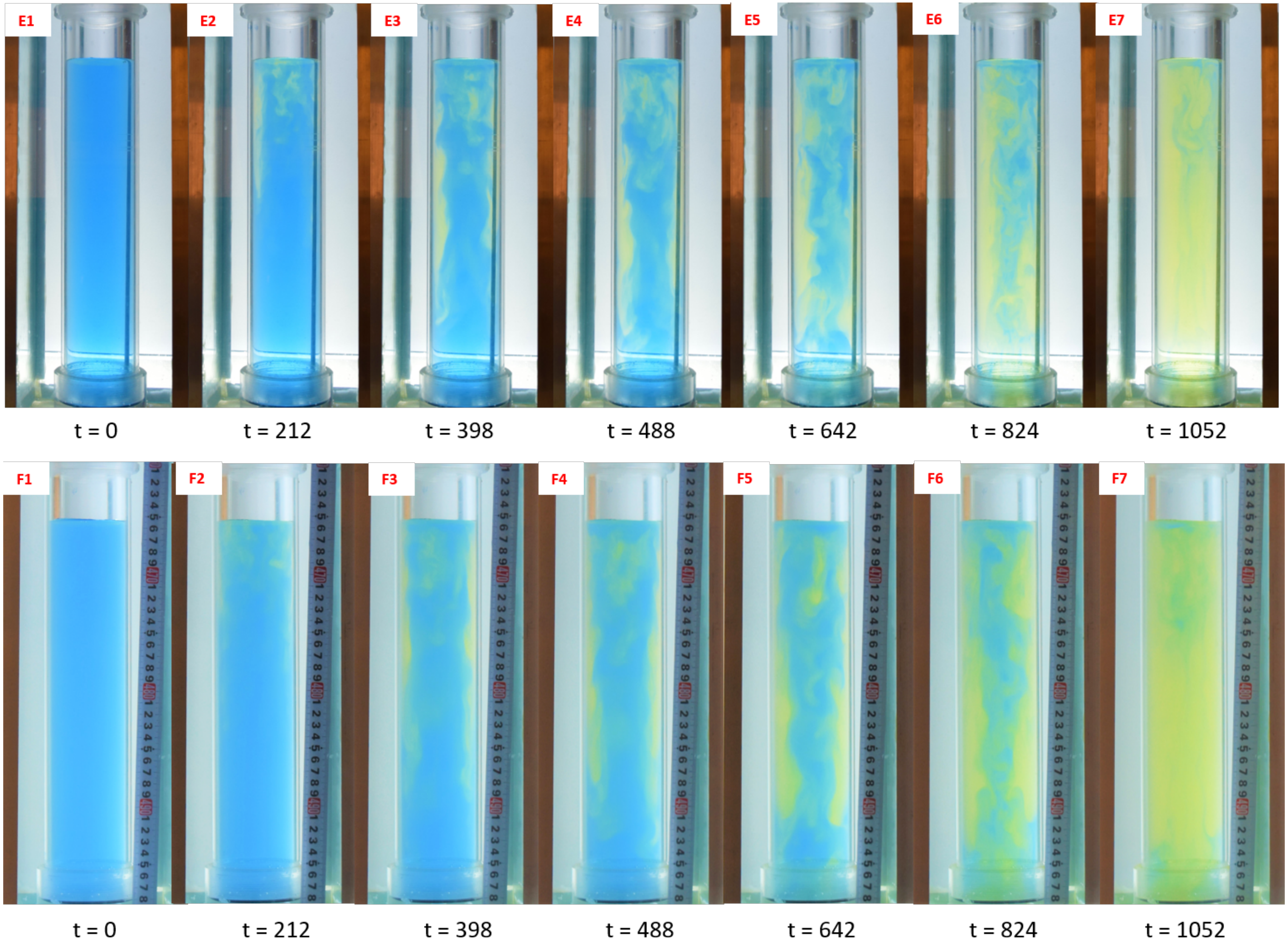

Figure 5.14: (*Exp* 5 *Base* + *NaCl*) - Visual observations of mixing regime by natural convection in saline WBS bulk volume. t [sec], y [mm]

5.3.3 Mixing Regime in 45% Porous Medium of 23800 mD Permeability

Spherical glass beads of 1 mm diameter were used to provide a unconsolidated, high porosity and permeability system in order to investigate the effects of porosity in a density-driven mixing regime. By combining a series of photos taken during two experiments with a nonsaline WBS, the propagation can be evaluated. At $t = 0$ the system is completely sealed off, whereas $y = 0$ is located at the gas liquid interface. From this reference point, all changes in the color indicator are assumed to be due to the convection flow as a result of increased CO_2 concentration within the liquid. A red dotted line has been added at the approximate displacement front, $y > 0$ given in mm, with increasing t given in minutes.

The propagation flow pattern of the yellow liquid was unique for each experiment, much like in the cases of bulk volume. Although Figure 5.15 show the exact same experiment of *Exp* 1 *Porous*, record with two cameras at 90° difference taken at approximately the same time[5], different mixing patterns were observed. Sequence *G* show clear finger-like displacement while sequence *H* show closer to a piston-displacement. Nevertheless, the rate of penetration at respective times were highly similar, showing a slow increase from 0 to approximately 1.16 mm/min.

Evaluating the mixing regime of *Exp* 2 *Porous* presented in Figure 5.16, the difficulty of repetability in the individual experiments becomes clear. At $t = 0$ the very first photo pair ($I1$ and $J1$) is affected by the implemented experimental procedure where CO_2 gas has dissolved into the solution. This was most probably caused due to bleeding off solution from the bottom of the cell during CO_2 injection, creating a type of suction effect through the matrix. The permeability doubles the injection time compared to the experiments performed in bulk volume. In addition, the liquid volume of unsaturated solution is reduced by 45% of maximal liquid volume, thereby less CO_2 is required to affect the initial pH significantly. Alternatively, if the beads or cell walls were insufficiently cleansed, residual CO_2 may have affecting the pH initially in the system. With each experiment performed, the pH was measured before (blue solution) and after (yellow solution) to ensure repeatability in the experimental procedure. The measured pH values are listed in Appendix C, where the *Blue* solution of *Exp* 2 *Porous* was much less compared to the other initial solutions.

Figure 5.17 shows *Exp* 2 *Porous* + *NaCl* performed in a saline WBS. Flow patterns similar to *Exp* 1 *Porous* are obtained, where clear fingers propagate in the downwards direction. However, the rate of penetration is highly varied, dependent on the photographed cross section, and with seemingly decreasing velocity. If compared to Figure 5.7, it is clear that salt had a direct impact on the mixing regime. Nonetheless, whether it is the salt alone decelerating the mixing regime,

---

[5] Due to technical difficulties with the cameras, the process was not captured until the end. In addition, picture $G2$ and $H2$ in Figure 5.15 were taken at 3 minute difference. However, the propagation in porous mediums are slow, therefore the error should be insignificant.

or if the situation is occurring in this experiment only is not easily ascertained. As observed in the previously discussed sequences, the mixing is unique. Therefore, visualization of mixing regime involving porous mediums and saline solutions should be further investigated. In addition, systems of lower porosity and/or permeability are of interest, regarding formations properties which may vary highly. Porosity and permeability are only two factors describing the formation quality, whereas mineralogy, consolidation and homogeneity are other critical factors affecting both diffusion and mixing regime.

In the case of bulk volume experiments it was claimed that the downwards flow was the dominating factor of the enhanced mass transfer mechanism. It was observed that the yellow fluid starts propagating in the radial direction only after reaching the bottom of the cell. In addition, some blue solution was observable in the uppermost section until the fluids were indistinguishable. Clearly, the situation is different when considering porous systems. Due to increased flow resistivity, the fingers are thicker and do not form macroscopic vortices. Nevertheless, the sequence in Figure 5.16 seem to grow mainly in the downwards direction before merging.

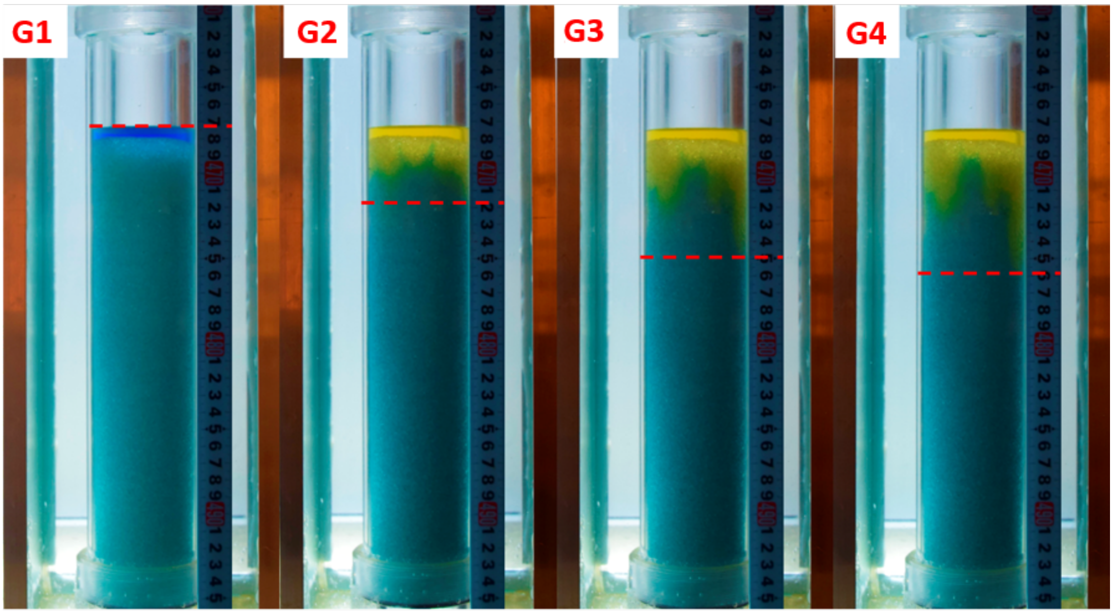

t = 0, y = 0   t = 45, y ≈ 42   t = 69, y ≈ 74   t = 79, y ≈ 83

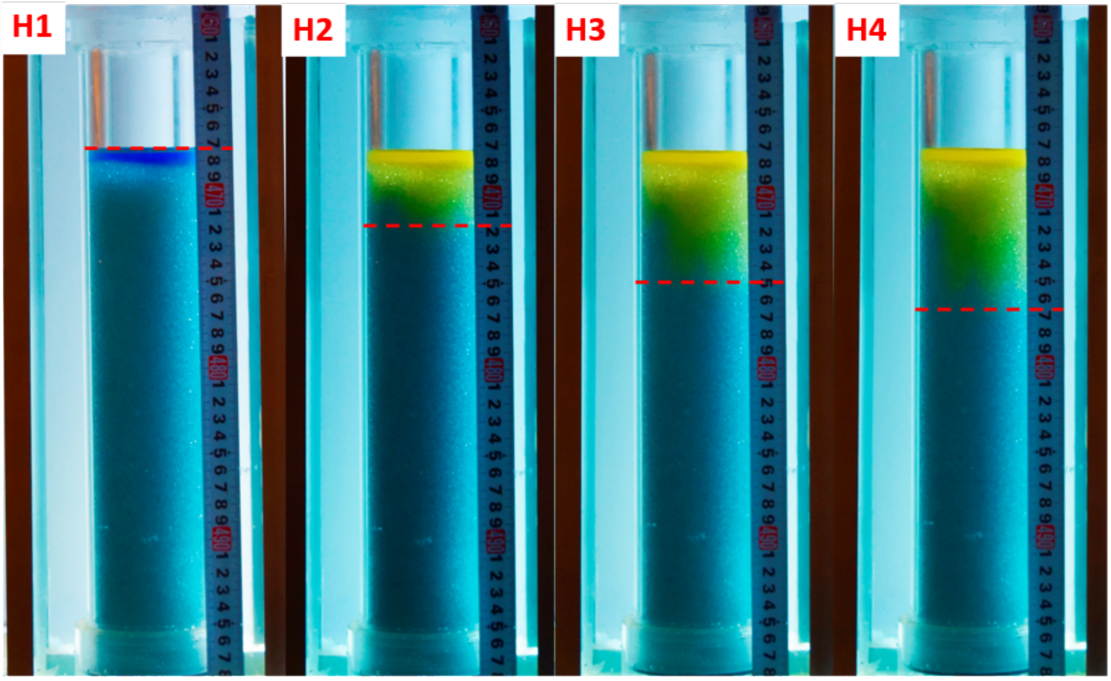

t = 0, y = 0   t = 42, y ≈ 45   t = 69, y ≈ 77   t = 79, y ≈ 92

Figure 5.15: (*Exp* 1 *Porous*) - Visual observations of enhanced mass transfer by convection driven flow in porous medium of 45% porosity and 23800 mD permeability. y [mm], t [min]

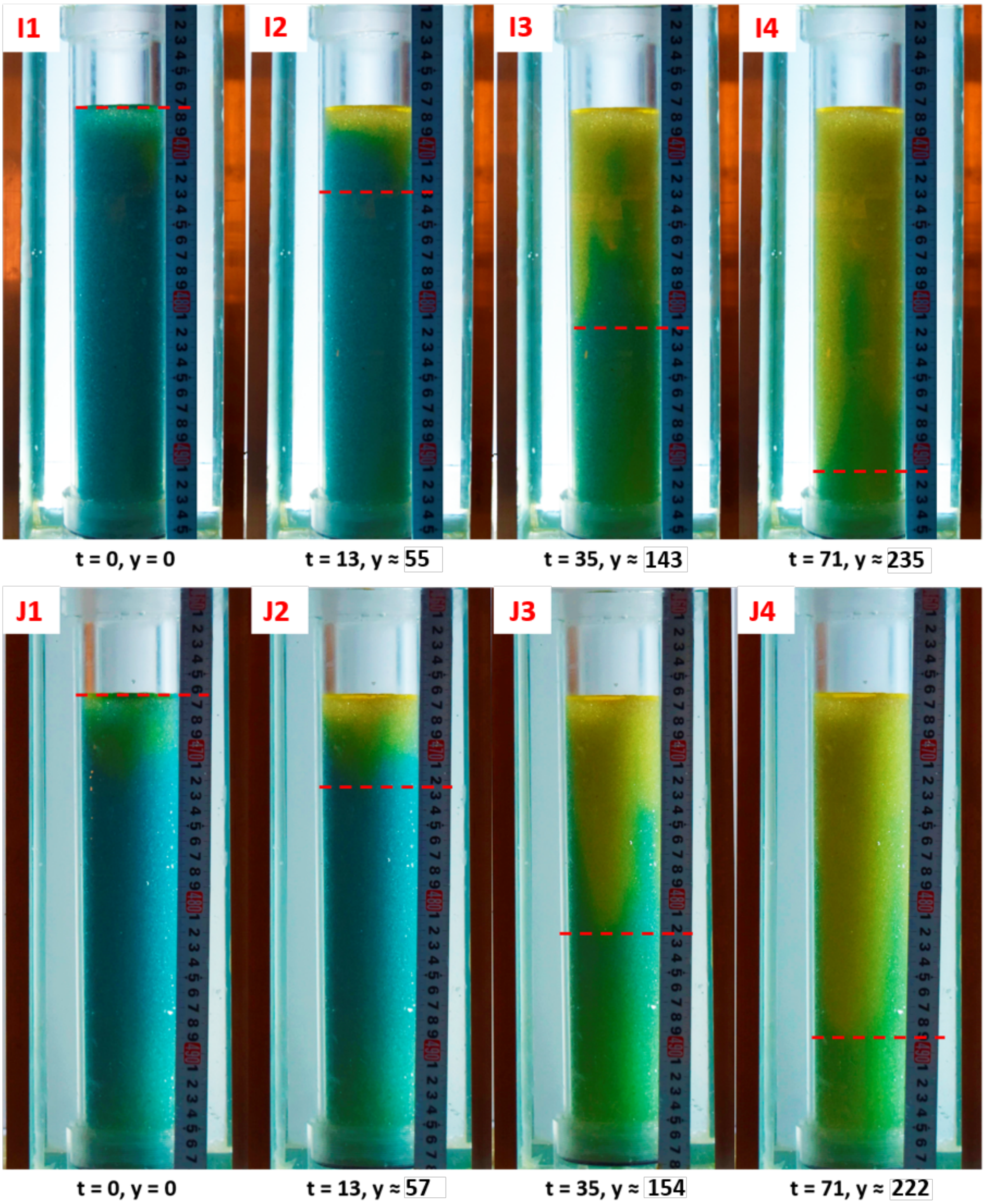

t = 0, y = 0 | t = 13, y ≈ 55 | t = 35, y ≈ 143 | t = 71, y ≈ 235

t = 0, y = 0 | t = 13, y ≈ 57 | t = 35, y ≈ 154 | t = 71, y ≈ 222

Figure 5.16: (*Exp* 2 *Porous*) - Visual observations of enhanced mass transfer by convection driven flow in porous medium of 45% porosity and 23800 mD permeability. t [min], y [mm]

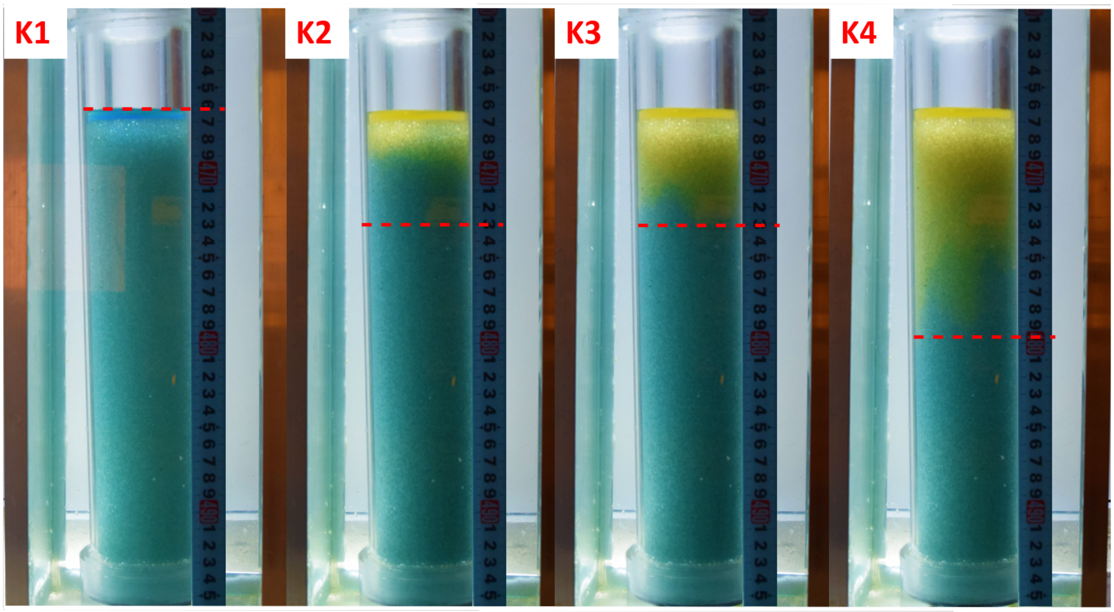

t = 0, y = 0 **t = 31, y ≈ 68** **t = 60, y ≈ 68** **t = 124, y ≈ 133**

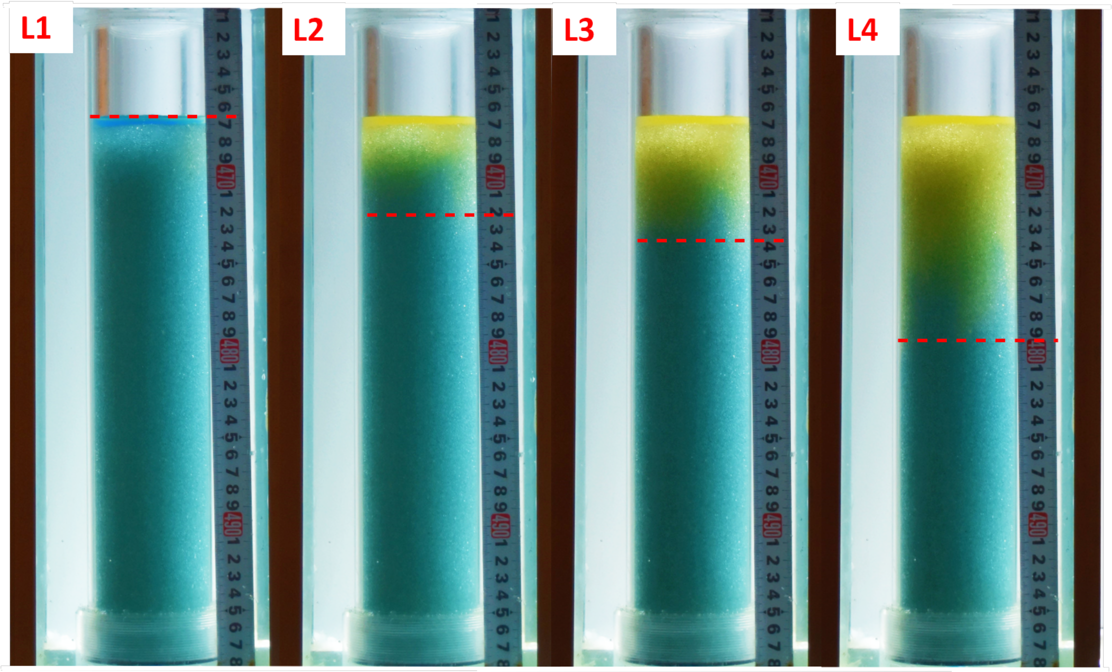

t = 0, y = 0 **t = 31, y ≈ 55** **t = 60, y ≈ 70** **t = 124, y ≈ 128**

Figure 5.17: ($Exp\ 2\ Porous{+}NaCl$) - Visual observations of enhanced mass transfer by convection driven flow in porous medium of 45% porosity and 23800 mD permeability in a saline WBS. t [min], y [mm]

5.4 Comparing Results from Bulk Volume and Porous Medium Experiments

Considering the saturation pressures in each case, it is noteworthy that only bulk volume experiments reach close to atmospheric pressure. This means there is sufficient liquid in the system for the gas to almost completely dissolve into. For sequestration purposes, this is important to consider regarding the time free phase CO_2 exist above the formation water and how much CO_2 is possible to dissolve. As in the case of *Exp 2 Base*, which was disregarded due to an insufficient P_0, indicated complete dissolution i.e. the gas dissolved into the solution completely without reaching P_{sat}. Hence, when planning geological storage the initial pressure should be sufficient to saturate the brine completely in order to utilise the formation to its fullest. At the time of writing, carbon storage is not commercialised. Therefore, when investing in sequestration project, the total amount of CO_2 which is feasible to store should be as high as possible without exceeding the storage capacity, and correspondingly the fracture pressure of the cap rock.

The nonsaline WBS for the porous system show identical diffusivity rates to the ones obtained from bulk volume, i.e. the order of magnitude is equal in all of the experiments at early and late time. However, the late diffusivity rate for the porous system with saline solution show a much slower rate, with as much as two orders of magnitude less than at early diffusion. The difference is noteworthy considering the time span free phase CO_2 exists in the formation. A high diffusivity rate will minimize the possibility of leakage into e.g. shallower formations or to the surface due to buoyancy, and is therefore favored.

More than 24.000 pictures were taken during the experiments. The picture series in this chapter were selected as representatives for bulk volume, capillary and porous medium experiments. The density driven mixing regime shows a significant contribution to the enhanced mass transfer when considering sequestration purposes. The effect is mainly dependent on the differences in density and the cell dimensions. In this study, the cell diameter and the change in density were relatively small, however, more than sufficient to observe the mixing regime. The visual measurements indicate that the lateral direction is favorable in both bulk volumes and in porous system, considering the fingers propagate mainly downwards before merging/growing sideways. The results indicate that the effect of mixing slows down and dies out after some time, i.e. when the solution turns yellow overall. The observations are supported by the pressure decay curves which show a constant decrease until reaching a saturation pressure. Figure 5.7 shows particularly the reduced effect of early diffusion when flow resisting parameters are introduced e.g. increased ionic strength.

6 Conclusion

Sequestration of CO_2 into deep geological aquifers has been proposed as a contribution to reduction of GHG. When supercritical CO_2 is pumped into the water bearing reservoir, a high pressure CO_2 plume will establish above the brine due to buoyancy. Consequently, a risk of leakage will be possible during the time there exist free phase CO_2 in the formation.

Pressure decay experiments were conducted inside a low pressure (5-7 bar) transparent cylinder-cell, to investigate the rate of diffusion of CO_2 gas into bulk volume and porous systems with nonsaline and saline WBSs. Due to the increased acidity of CO_2(aq), a pH indicator was added to the solutions, thereby allowing visual observations of the transport mechanisms occurring in the experiments. To study the rate of diffusion from the experiments conducted, a suitable pressure decay model was derived. For sequestration purposes, the dissolution mechanisms can be investigated by analytical models ranging from very simple to quite complex, depending on the defined interface boundary conditions and fluids used. The boundary conditions in this study were selected to keep calculations simple while maintaining high accuracy regarding the measurements. The model was applied with the collected pressure data from the experiments to obtain saturation pressures and diffusion coefficients. In addition, visual interpretations of the mixing regime caused by the enhanced mass transfer mechanism were discussed. This was done in order to understand the contribution of the early and late time convection dominated diffusion of CO_2 into the solutions.

The model was evaluated for each set of experiments, where the diffusion constant in both nonsaline and saline bulk volume experiments showed identical relation in the order of magnitude. This was also true for porous systems performed with nonsaline WBS. However, a noticeable exception was obtained when an experiment was performed with the combination of saline WBS with the porous system. The contribution from the enhanced mass transfer was reduced, resulting in a much longer late diffusion time span. This is assumed to be caused by the increased ionic strength from NaCl. It is noteworthy that the concentration of salt is considerably small for these experiments, 38.4 g NaCl/L DW, nevertheless resulting in high differences. When considering carbon storage in saline aquifers, a high diffusivity rate is desirable. The effect of increased salinity and the presence of organic and inorganic substances may highly reduce the diffusivity, and consequently the possible amount of sequestrated CO_2.

The saturation pressure for each experiment was obtained analytically, indicating the amount of CO_2 left in the gas column above the solution. Considering the polarity of the components, a sufficient amount of water is required to dissolve CO_2 completely. A saturation pressure close to the ambient pressure was only reached in the experiments involving bulk volumes whereas in the experiments involving porous system, P'_{sat} was approximately twice. Obtaining a high P_{sat}

indicates free phase CO_2 still existing in the gas column. The observation can be related to carbon storage, where free phase CO_2 can leak into shallower formations or to the surface due to buoyancy. A cap rock that fulfills the requirements of desired geometry and properties is therefore needed to prevent any unwanted migration of CO_2. However, obtaining low P_{sat} value (dependent on the system investigated e.g. values below ambient pressure) indicate that saturation was not achieved. The pressure data applied with the derived model implemented that a minimum initial pressure was required to sufficiently saturate the solution. Considering the cost of sequestration, it is important to utilize the formation to its fullest potential without exceeding the storage capacity or fracture pressure of the cap rock.

The results from the pressure decay curves showed three stages of diffusivity with each experiment performed. Initial diffusion occurred only in a short period at the uppermost liquid layer before early- and late convection dominated diffusion started. The latter two were of highly interest considering the instability occurring at the interface due to gravitational effects, forming finger-like flow in the lateral direction. The convection flow showed a significant contribution to the enhanced mass transfer mechanism. In all the experiments the lateral direction was favourable, where the fingers propagated mainly downwards before merging or expanding in the horizontal direction. With time, the effect from mixing slows down as the solution becomes saturated. The observation is important regarding safe and protracted storage of CO_2, where the risk of leakage is highly reduced.

References

Allen, M.R. et al. (2018). *Framing and Context. In: Global Warming of 1.5C. An IPCC Special Report on the impacts of global warming of 1.5C above pre-industrial levels and related global greenhouse gas emission pathways, in the context of strengthening the global response to the threat of climate change, sustainable development, and efforts to eradicate poverty.* Accessed on March 4th, 2020. URL: `https://www.ipcc.ch/sr15/chapter/chapter-1/`.

Anton Paar Instruction Manual DMA 4100 M, DMA 4500 M, DMA 5000 M (2012).

Bentham, Michelle and Mg Kirby (2005). "CO2 Storage in Saline Aquifers". In: 60, pp. 559–567. DOI: `10.2516/ogst:2005038`.

Bjorlykke, Knut (2015). *Petroleum Geoscience : From Sedimentary Environments to Rock Physics.* eng. Berlin, Heidelberg.

Çengel, Yunus A. (2012). *Fundamentals of thermal-fluid sciences.* eng. 4th ed. in SI units. McGraw-Hill higher education. New York, N.Y: McGraw-Hill, p. 998. ISBN: 9780071325110.

CO2 Earth (2020). *Earth's CO2 Home Page.* Accessed on June 13th, 2020. URL: `https://www.co2.earth/`.

Cook, Andrew and David Youngs (Jan. 2009). "Rayleigh-Taylor instability and mixing". In: *Scholarpedia* 4, p. 6092. DOI: `10.4249/scholarpedia.6092`.

Di Gianfrancesco, Augusto (2016). *Materials for ultra-supercritical and advanced ultra-supercritical power plants.* Accessed on March 4th, 2020. Woodhead Publishing, p. 676. URL: `https://books.google.no/books?id=l4d4CgAAQBAJ&lpg=PP1&ots=vhgkT_AibW&dq=Materials%20for%20Ultra-Supercritical%20and%20Advanced%20Ultra-Supercritical%20Power%20Plants&lr&hl=no&pg=PA676#v=onepage&q=key%20part%20to%20play&f=false`.

Engineers Edge (2020). *Water - Density Viscosity Specific Weight.* Accessed on June 13th, 2020. URL: `https://www.engineersedge.com/physics/water__density_viscosity_specific_weight_13146.htm`.

Farajzadeh, R. et al. (2007). "ENHANCED TRANSPORT PHENOMENA IN CO2 SEQUESTRATION AND CO2 EOR". PhD thesis in Petroleum Engineering. Delf, The Netherlands: Delft University of Technology.

Hydroxide (2017). In: *Encyclopædia Britannica.* Accessed on March 12th, 2020. Encyclopædia Britannica, inc. URL: `https://www.britannica.com/science/hydroxide`.

Kelland, Malcolm A. (2019). Personal communication.

Khosrokhavar, Roozbeh et al. (2014). "Visualization and investigation of natural convection flow of CO2 in aqueous and oleic systems". In: *Journal of Petroleum Science and Engineering* 122, pp. 230–239. ISSN: 0920-4105. DOI: `https://doi.org/10.1016/j.petrol.2014.07.016`. URL: `http://www.sciencedirect.com/science/article/pii/S0920410514002149`.

Metz, B. et al. (2005). *IPCC, 2005: IPCC Special Report on Carbon Dioxide Capture and Storage.* In: Accessed on March 4th, 2020. Cambridge University Press, Cambridge, United Kingdom and New York, NY, USA. URL: `https://www.ipcc.ch/site/assets/uploads/2018/03/srccs_wholereport-1.pdf`.

Ministry of Petroleum and Energy (2016). *Initiates feasibility study on subsea CO2 storage.* Accessed on June 11th, 2020. URL: `https://www.regjeringen.no/en/aktuelt/statoil-skal-utgreie-co2-lager-pa-norsk-kontinentalsokkel/id2469150/`.

Nazari Moghaddam, Rasoul et al. (2012). "Quantification of Density-Driven Natural Convection for Dissolution Mechanism in CO 2 Sequestration". eng. In: *Transport in Porous Media* 92.2, pp. 439–456. ISSN: 0169-3913.

Norwegian Petroleum (2020). *Carbon capture and storage.* In: Accessed on April 7th,2020. URL: `https://www.norskpetroleum.no/en/environment-and-technology/carbon-capture-and-storage/#main-content-start`.

Osman, Mohamad (2011). *Chemistry.* eng. Custom Book Edition. Pearson Education, pp. 12–14. ISBN: 9780857764546.

Rabenjafimanantsoa, A.H. and Svein Myhren (2019). *Dynamiske målinger av porsitet og permeabilitet.* In: *Laboratorieøvinger i PET120 Reservoarteknikk.* Department of Petroleum Engineering at the University of Stavanger.

Rackley, Stephen A. (2017). *Carbon Capture and Storage.* Accessed on March 9th, 2020. Oxford, UNITED STATES: Elsevier Science Technology, p. 131. ISBN: 9780128120422.

Riazi, Mohammad R. (1996). "A new method for experimental measurement of diffusion coefficients in reservoir fluids". eng. In: *Journal of Petroleum Science and Engineering* 14.3-4, pp. 235–250. ISSN: 0920-4105.

Specific gravity (2018). In: *Encyclopædia Britannica.* Accessed on March 23th, 2020. Encyclopædia Britannica, inc. URL: `https://www.britannica.com/science/specific-gravity`.

Spinelli, C. M. et al. (n.d.). *CO2 Pipeline Transportation New Needs.* In: International Society of Offshore and Polar Engineers.

Spiro, Thomas G., Kathleen L. Purvis-Roberts, and Williams M Stagliani (2012). *Chemistry of the environment.* 3rd ed. Sausalito, Calif.: University Science Books. ISBN: 9781891389702.

Tetthet og relativ tetthet av gass. (2019). In: *Produksjon av olje og gass - Laboratoriehefte PET 200.* Department of Petroleum Engineering at the University of Stavanger.

The Editors of Equinor (2018). *Equinor Climate Roadmap Creating a low carbon advantage.* Accessed on March 4th,2020. URL: `https://www.google.no/url?sa=t&rct=j&q=&esrc=s&source=web&cd=1&cad=rja&uact=8&ved=2ahUKEwi0r7j4i8foAhUhlYsKHdBdDQwQFjAAegQIARAB&url=https%3A%2F%2Fwww.equinor.com%2Fcontent%2Fdam%2Fstatoil%2Fimage%2Fhow-and-why%2Fclimate%2Fclimate-roadmap-2018-digital.pdf&usg=AOvVaw1xZPN_ofNQ7iHHGJrufuSF`.

The University of Utah's College of Engineering (n.d.). *Lecture 4: Diffusion: Fick's second law.* Accessed on June 13th, 2020. URL: `https://www.google.com/url?sa=t&rct=j&q=&esrc=s&source=web&cd=&cad=rja&uact=8&ved=2ahUKEwi26JvwwtbqAhVSx4sKHSTbDs0QFjAAegQIAxAB&url=http%3A%2F%2Fwww.eng.utah.edu%2F~lzang%2Fimages%2Flecture-4.pdf&usg=AOvVaw2pq3Rebo40eXCm3xravwwS`.

Tveteraas, Ørjan (2011). "A Study of Pressure Decay in a Closed CO2-water System". Master thesis in reservoir engineering. Stavanger, Norway: University of Stavanger.

Youngs, David L (1991). "Three-dimensional numerical simulation of turbulent mixing by Rayleigh–Taylor instability". eng. In: *Physics of Fluids A: Fluid Dynamics* 3.5, pp. 1312–1320. ISSN: 0899-8213.

Zarghami, Shahin, Fathi Boukadi, and Yahya Al-Wahaibi (2016). "Diffusion of carbon dioxide in formation water as a result of CO2 enhanced oil recovery and CO2 sequestration". eng. In: *Journal of Petroleum Exploration and Production Technology* 7.1, pp. 161–168. ISSN: 21900558. URL: `http://search.proquest.com/docview/1869046687/`.

A CO$_2$ Density and Specific Gravity

An effusiometer was used to measure the effusion time of CO$_2$ gas of 99.99% purity. The measurements and calculations are based on Graham's law of effusion:

$$\frac{rate_{ref}}{rate_{gas}} = \sqrt{\frac{M_{gas}}{M_{ref}}} = \frac{t_{gas}}{t_{ref}} \tag{A.1}$$

where the rate is given in volume per unit time and M is the molecular weight of the individual components. Since the effusion of gas and the reference gas (denoted by ref) occurs in the same volume, but with different durations, the rate can be regarded simply as time. Table A.1 shows the measured time of effusion for CO$_2$ gas and the reference gas, which in this case is air:

Table A.1: Measured effusion time of CO$_2$ and air [MM.SS.SSS].

	t_{CO2}	t_{air}
1	01.17.46	00.59.05
2	01.17.80	00.59.86
3	01.17.54	00.59.36
4	01.17.27	01.00.72
5	01.17.69	01.00.83
average	01.17.55	00.59.96

The specific gravity γ can be calculated from the following equation when $t_1 = t_2$ and $P_1 = P_2$:

$$\gamma_{t_2/t_1, P_2/P_1} = \gamma = \frac{\rho_{gas}}{\rho_{air}} \tag{A.2}$$

where ρ_{air} =1.19 Kg/m^3 at P = 755.687 $mmHg$ and T = 21°C is found by:

$$\rho_{air} = \frac{1.293}{1 + 0.00367 \cdot T} \cdot \frac{P}{760} \tag{A.3}$$

Introducing the equation of kinetic energy $\frac{1}{2} m_1 v_1^2 = \frac{1}{2} m_2 v_2^2$, Equation (A.2) can be related to Equation (A.1) in the following way:

$$\frac{v_2^2}{v_1^2} = \frac{m_1}{m_2} = \frac{\rho_1}{\rho_2}\frac{V}{V} \qquad \longrightarrow \qquad \frac{t_{gas}^2}{t_{air}^2} = \frac{\rho_{gas}}{\rho_{air}} = \gamma \tag{A.4}$$

where V is an arbitrary unit volume. Applying the average time of effusion from Table A.1 into Equation (A.4) gives $\gamma_{CO2} = 1.673$, and with the same formula $\rho_{CO2} = 1.99\ Kg/m^3$.

B Porosity and Permeability of Unconsolidated Matrix

A small diameter glass tube of $A = 10$ mm and length $L = 450$ mm packed with the desired matrix material can be used to measure both permeability and porosity. The complete system for both measurements is illustrated in Figure 4.2 where v^1, v^2 and v^3 are valves at their closed position. This measurement allows a higher grade of compaction, compared to a static measurement by, for instance, a graduated cylinder. However, it is important to mention that visual estimates can affect the results. Therefore, the procedures are repeated at different rates q and pressures P.

The porosity is measured by injecting a small amount of color (lissamin rot) at the inlet of the glass tube by opening valve v^2. As the colour is pumped through the waterwett matrix, the time and displacement is measured. To verify the measurements the experiment is repeated at different rates until comparable results are achieved. The measured values of displacement are then plotted against time, and a linear curve fit is used to obtain the gradient dx/dt in each set of measurements:

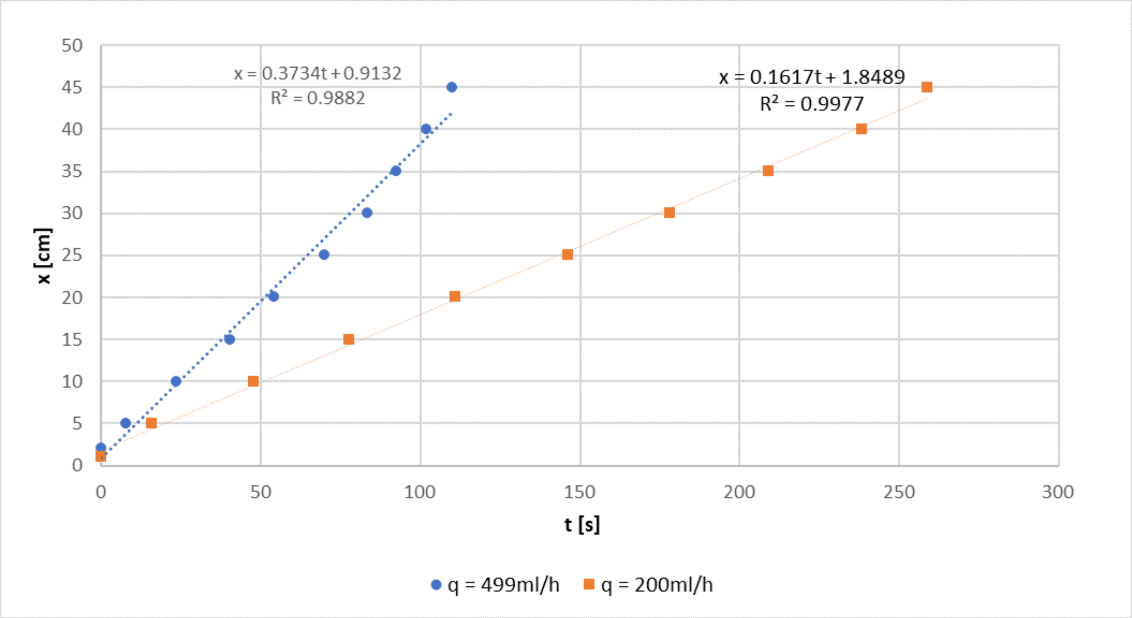

Figure B.1: Displacement vs. Time for 1mm Porous Media.

Equation (B.1) can then be applied for each data sett to calculate the porosity:

$$q = \phi A \frac{dx}{dt} \qquad \longrightarrow \qquad \phi = \frac{q}{A}\left(\frac{dx}{dt}\right)^{-1} \tag{B.1}$$

The calculated porosity from $q = 499\ ml/h$ and $q = 200\ ml/h$ measurements of the glass beads with average 1 mm diameter was found to be approximately 47.3% and 43.7% respectively.

When measuring the permeability, v^2 is closed. A flask is hung above the system at an height h_n, and connected at the inlet of the glass tube containing the matrix material. The flask should have a constant volume at all time during the experiment in order to provide a constant hydrostatic pressure into the glass tube at all time. This is possible by pumping water in to the flask through opening v^1 as well as allowing excess water to seep out when maximum volume is reached. The pressure is also controlled by an external pressure sensor to avoid bias. The experiment starts when v^3 is turned to open and the first drop of water seeps out from the glass tube outlet. The rate of water going through the matrix is found by measuring the time t and a reference outlet water volume V. The experiment is repeated at different h_n. The measured results are summarised in Table B.1:

Table B.1: Measurements Permeability

h_n $[cm]$	V $[ml]$	t $[s]$	q $[\frac{ml}{s}]$	P $[bar]$
175	3.0	780	0.0038	0.1703
150	3.5	1800	0.0019	0.1455
125	1.2	960	0.0013	0.1217
100	1	1151	0.0009	

By plotted the rate against h_n, a linear curve fit can be obtained in order to find the gradient q/h_n:

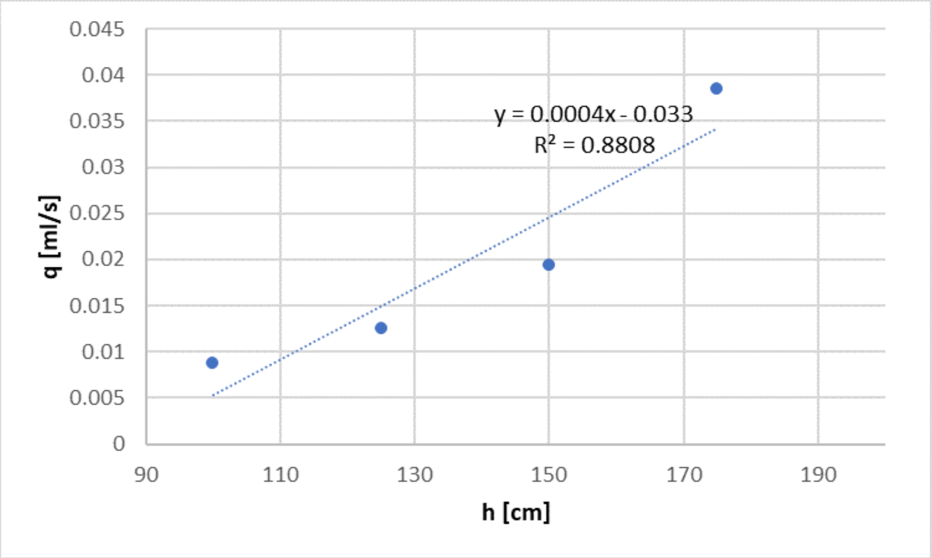

Figure B.2: Rate vs. hydrostatic pressure height for 1mm Porous Media.

The permeability of the matrix can then be calculated by Darcy's law:

$$q = \frac{kA}{\mu} \frac{\rho g h_n}{\Delta l P_{atm}} \qquad \longrightarrow \qquad k = \frac{\mu \Delta l P_{atm}}{A} \frac{q}{h_n} \tag{B.2}$$

where A and Δl are the tube area and length, respectively, ρ and μ are the water properties, g is the gravitational acceleration constant and P_{atm} is the atmospheric pressure. The calculated permeability for the glass beads of 1mm average diameter was found to be approximately 23.8 D.

C Fourier Analysis: Derivation of a_n

Fick's second law describes the concentration of gas as it defuses into a liquid solution column of a given height y, during a time period t.

$$\frac{\partial c(y,t)}{\partial t} = D\frac{\partial^2 c(y)}{\partial y^2} \tag{C.1}$$

where D is the constant diffusion coefficient for a given pair of species in $[m^3/s]$ at constant temperature. By applying Fourier analysis, the variables are evaluated separately, providing infinitely many distinct solutions of Fick's second law at the predefined boundaries:

$$c(t,y) = a_m exp\left(\frac{-t}{\tau_m}\right) sin(\kappa_m y) \tag{C.2}$$

Due to the linearity of Fick's second law, the most general solution to Equation (C.2) will be a superposition of all the specific solutions given by the infinite sum:

$$c(t,y) = a_0 + \sum_{n=0}^{\infty} a_n exp\left(\frac{-tD(2n+1)^2\pi^2}{4L^2}\right) sin\left(\frac{(2n+1)\pi y}{2L}\right) \tag{C.3}$$

Where a_0 is determined from the initial data at the upper boundary:

$$c(t, y=0) = a_0 = c_{sat} \tag{C.4}$$

and a_n is determined by the gas concentration in the liquid column $0 < y < L$ at $t = 0$:

$$c(t=0,y) = a_0 + \sum_{n=0}^{\infty} a_n sin\left(\frac{(2n+1)\pi y}{2L}\right) \tag{C.5}$$

Both sides of Equation (C.5) are multiplied by the sin mode $sin((2m+1)\pi y/2L)$ and integrated over the domain:

$$\int_0^L c(t=0,y) sin\left(\frac{(2m+1)\pi}{2L}\right) dy =$$

$$a_0 \int_0^L sin\left(\frac{(2m+1)\pi y}{2L}\right) dy + \sum_{n=0}^{\infty} a_n \left[\int_0^L sin\left(\frac{(2m+1)\pi y}{2L}\right) sin\left(\frac{(2n+1)\pi y}{2L}\right) dy\right] \tag{C.6}$$

The left hand side of Equation (C.6) simply becomes zero due to the fact that there is no gas in the liquid solution at initial conditions. In addition, the only valid result is obtained when $m = n$:

$$0 = a_0 \int_0^L sin\left(\frac{(2n+1)\pi y}{2L}\right) dy + \sum_{n=0}^{\infty} a_n \left[\int_0^L sin^2\left(\frac{(2n+1)\pi y}{2L}\right) dy\right] \tag{C.7}$$

which yields:

$$0 = a_0 \left(\frac{-2L}{(2n+1)\pi}\left[cos\left(\frac{(2n+1)\pi y}{2L}\right)\right]_0^L\right) + \sum_{n=0}^{\infty} \frac{a_n}{2}\left(y - \frac{L}{(2n+1)\pi}\left[sin\left(\frac{(2n+1)\pi y}{L}\right)\right]_0^L\right) \tag{C.8}$$

When evaluated at the boundaries, a simple solution of a_n is left:

$$a_n = -a_0 \frac{4}{(2n+1)\pi} \tag{C.9}$$

D pH Values from Experiments

In order to evaluate the transport mechanisms occurring when CO_2 dissolves into water and in order to determine the amount of gas dissolved in each experiment, alkaline solutions were prepared with the following quantities and characteristics:

Table D.1: Solution Base Recipe

Compound	*Amount*	*Property*
Deionized water (DW)	5 L	pacificated water
5% Sodium hydroxide (NaOH)	3.75 ml	strong base solution
Bromothymol blue (BTB)	35 ml	pH indicator

The volume of each batch is enough to perform the experiments maximum 3 times. However, it was decided to use the solute remnants to cleans the cell walls and glass beads after rinsing with DW to reduce dilution. pH measurements were taken before and after each experiment with a METTLER TOLEDO SevenCompact pH-meter at average room temperature of 19.5°C. The chosen pH indicator has a transition range between pH 6.0 and pH 7.6 where the solution is yellow at acidic conditions and blue at alkaline.

In order to investigate the effect saline brine may have on the storage capacity of CO_2, experiments were conducted with the same solution as the one provided in Table D.1, but with adding 38.4 grams of NaCl per liter of DW before adding NaOH and BTB. The salt provides an ionic strength of 0.657 M.

Batch AW, BW, CW and AS were applied in bulk volume experiments, thus the blue solutions were only pH tested before pumping into the cell. However, the yellow solution is dependent on the initial pressure of each experiment and was therefore tested shortly after extraction. Batch DW and BS were applied in porous mediums. Due to increased surface area the solutions may have been affected due to CO_2 residuals and was therefore pH tested after solution extraction from the bottom of the cell during CO_2 injection. As can be seen from Table D.3, the blue solution of the second experiment performed with DW has a much less pH compared to the first, although performed with the same solution. Because of this the washing routine of the glass beads was slightly changed from simply washing with DW and correlated blue solution, to addition of increased NaOH washing in between these two steps. The pH of the blue saline solutions (AS and BS) show close to average values anew.

Table D.2: Solution pH before and after experiment, prepared from Solution Base Recipe

Experiment label	*DW*	*Blue*	*Yellow*
Exp 1 Base	5.91	11.20	5.25
Exp 2 Base	5.91	11.20	5.03
Exp 3 Base	5.91	11.20	4.88
Exp 1 Capillary	5.90	11.34	5.04
Exp 2 Capillary	5.90	11.34	5.04
Exp 1 Porous	5.86	11.50	5.59
Exp 2 Porous	5.86	7.79	5.33

Table D.3: Solution pH before and after experiment, prepared from Solution Base Recipe with the addition of 38.4 g NaCl/L

Batch label	$DW + NaCl$	*Blue*	*Yellow*
Exp 1 Base+NaCl	5.92	9.30	4.73
Exp 2 Base+NaCl	5.92	9.30	4.71
Exp 1 Porous+NaCl	8.63	10.69	5.26
Exp 2 Porous+NaCl	8.63	11.08	6.00